Journal of Computational Physics 227 (2008) 8268–8289

Contents lists available at ScienceDirect

Journal of Computational Physics

journal homepage: www.elsevier.com/locate/jcp

Asymptotic and numerical analysis of an inviscid bounded vortex flow at low Mach number

Anne Cadiou *, Lionel Le Penven, Marc Buffat

Université de Lyon, CNRS, École Centrale de Lyon, Insa de Lyon, Université de Lyon 1, Laboratoire de Mécanique des Fluides et d'Acoustique, 36, av. Guy de Collongue, F-69134 Ecully, France

ARTICLE INFO

Article history:
Received 26 July 2007
Received in revised form 29 April 2008
Accepted 22 May 2008
Available online 10 June 2008

Keywords:
Compressible low Mach number flow
Explicit Roe scheme
WENO and high-order-compact schemes
Implicit scheme
Asymptotic development

ABSTRACT

The inviscid low Mach number compressible flow developing from a plane incompressible vortex with constant density in a bounded domain is studied. A reference solution for this model flow is obtained by two-time scale asymptotic development in the zero Mach number limit. The solution can be decomposed into variations with a slow convective and a fast acoustic time scale. A selection of numerical schemes widely used to solve unsteady compressible low Mach number flows has been implemented to simulate this flow for two Mach number values, $M = 0.1$ and $M = 0.01$. The ability of the schemes to predict low Mach number flows and their behavior with the value of the Mach number have been analyzed.

1. Introduction

In the last two decades, significant progress has been made in the mathematical study of the low Mach number limit of the compressible Euler and Navier–Stokes equations [48]. Since the pioneering work of Klainerman and Majda [29] for Euler isentropic flows and nearly incompressible initial data, rigorous results have been established with more general hypotheses, considering the case of general initial data [4,25], non-isentropic flows [39] and for bounded or unbounded domains [2]. Recent developments consider the incompressible limit for the Navier–Stokes equations [32,34,20].

In parallel to the mathematical studies, obtaining accurate numerical solutions of compressible low Mach number flows is also the subject of many investigations. When the Mach number is very small, the time scale linked to the propagation of acoustic waves becomes very small compared to the time scale associated to characteristic velocities of the flow, leading to a degradation in efficiency and accuracy of the method of resolution [11,37]. Two strategies are generally adopted.

The first one consists in solving an approximated system of equations obtained by an asymptotic decomposition at low Mach number of the compressible equations. This decomposition allows the equations linked to the respective distinct characteristic scales to be resolved by different methods. The separation of the scales allows the transition from a hyperbolic system of compressible equations to a hyperbolic/elliptic one in the low Mach number limit to be distinguished. The method can eliminate the acoustic contribution while allowing weak compressibility effects due to source terms or transport phenomena to be represented [35]. This approach is retained for example for variable density flows due to stratification [10] or thermal transfers [42]. It is widely used for a large range of low Mach number applications in combustion, multi-phase or thermodynamical flows, but the methods used for one application are not always valid for another. The major difficulty lies

* Corresponding author.
E-mail address: anne.cadiou@ec-lyon.fr (A. Cadiou).

0021-9991/$ - see front matter © 2008 Elsevier Inc. All rights reserved.
doi:10.1016/j.jcp.2008.05.024

in the fact that the decomposition is far from being unique [31]. The numerical method developed for one decomposition remains largely associated to the validity domain of the approximated equations [40]. Despite many differences in the detail, most of the numerical methods retain the same strategy, derived from the resolution of the incompressible equations, and referred to as pressure-based methods by Keshtiban et al. [28]. These methods belong to the class of predictor–corrector methods where the acoustic pressure is calculated once the convective flow has been estimated.

When the validity of the approximated system is no longer satisfied, for example when the Mach number increases in time or locally in the flow, this strategy cannot be retained. This occurs for example in the transition from deflagration to detonation [6] or in cavitation flows [7] where locally supersonic bubbles exist in an otherwise subsonic flow. In a general way scale separation is not suited to flows where the propagation of acoustic waves or thermodynamic coupling plays a dominant role, as in the formation of thermoacoustic instabilities [22]. The second strategy consists therefore in solving the compressible fluid mechanics equations with numerical methods inspired by the resolution of high speed flows, and referred to as density-based methods by Keshtiban et al. [28], where modifications are made in order to compensate for the poor efficiency and the lack of precision in the low Mach number limit [16]. The fact that the acoustic wave velocity is large compared to the convective velocity decreases the efficiency of the explicit compressible methods in the low Mach number limit because the stability criteria require the use of very small time steps [23]. This limitation can become very severe in the case of unsteady flows and can also reduce the accuracy of the solution. On the other hand, implicit methods can be cumbersome because of the ill-conditioned system to solve [46]. To deal with the scale discrepancy, compressible methods are usually preconditioned [55]. The method proposed by Turkel [54] accelerates the convergence of steady flows by modifying the time step. This kind of method is known to introduce numerical dissipation, which reduces accuracy in unsteady flows [59]. The use of a dual time step extends these approaches to time-dependent flows [12] for which all the frequencies need not be predicted. These density-based strategies modify the properties of the numerical schemes and the pertinence of those approaches for long time integration such as required by DNS and LES simulations remains a particular issue.

The reason for this work is to analyze the low Mach number behavior of a selection of numerical schemes usually applied to such compressible simulations, with separate time and space integration, and derived from Godunov's type of scheme. This work focuses on the compressible Euler equations and the study of the numerical methods is performed with the help of asymptotic expansion of a model flow consisting of incompressible initial vortex in a bounded domain.

The governing compressible equations are introduced in Section 2. Dimensionless equations are presented together with the model flow configuration retained in this study. Numerical methods are described in Section 3. The low Mach number solution of the model flow is analyzed in Section 4 using an asymptotic expansion in the zero Mach number limit. Numerical simulations are compared in Section 5 with respect to their low Mach number behavior, their accuracy and stability properties. Concluding remarks are given in Section 6.

2. Governing equations

In order to analyze the behavior of numerical schemes at low Mach number flows, a simple yet non-trivial model flow is considered, consisting of a plane inviscid vortex evolving inside a bounded domain $\Omega = [0,L] \times [0,L]$.

The flow is governed by the compressible Euler equations where conservation of mass, momentum and total energy are given in a conservative form by

$$\frac{\partial \rho}{\partial t} + \nabla \cdot (\rho \mathbf{u}) = 0 \tag{1a}$$

$$\frac{\partial \rho \mathbf{u}}{\partial t} + \nabla \cdot (\rho \mathbf{u} \otimes \mathbf{u}) + \nabla p = 0 \tag{1b}$$

$$\frac{\partial \rho e_t}{\partial t} + \nabla \cdot ((\rho e_t + p)\mathbf{u}) = 0 \tag{1c}$$

where ρ denotes the density, $\mathbf{u}$ the velocity, p the pressure and e_t the total energy, defined by $\rho e_t = \rho e + \frac{1}{2}\rho \mathbf{u}^2$ in terms of the internal energy e. The flow follows the ideal gas law so that the pressure and the internal energy are related by the following equation of state:

$$p = (\gamma - 1)\rho e \tag{2}$$

where γ is the heat capacity ratio.

A non-dimensionalization of the equations is performed by using the basic reference values of length, density, fluid velocity and pressure, L_{ref}, ρ_{ref}, u_{ref} and p_{ref}. The low Mach number limit of the Euler equations can be expressed by choosing different reference values for the flow velocity and the sound velocity, respectively u_{ref} and c_{ref}. The reference Mach number

$$M = \frac{u_{\text{ref}}}{c_{\text{ref}}} \tag{3}$$

determines a thermodynamic pressure $p^{\text{t}}_{\text{ref}}$, according to the definition of the reference sound speed

$$c_{\text{ref}} = \sqrt{\frac{\gamma p^{\text{t}}_{\text{ref}}}{\rho_{\text{ref}}}} \quad \text{so that } p^{\text{t}}_{\text{ref}} = \frac{\rho_{\text{ref}} u^2_{\text{ref}}}{\gamma M^2} \tag{4}$$

with a density reference ρ_{ref}. Another choice can be made for the pressure reference, based on a dynamical pressure reference $p^{\text{d}}_{\text{ref}}$ defined as

$$p^{\text{d}}_{\text{ref}} = \rho_{\text{ref}} u^2_{\text{ref}} \tag{5}$$

to scale the pressure gradient in the momentum equation. If the thermodynamic reference pressure is retained, the dimensionless pressure is defined by

$$p = p^{\text{t}}_{\text{ref}} p^+ \tag{6}$$

whereas in the other case, it will be defined as

$$p = p^{\text{d}}_{\text{ref}} p^* \tag{7}$$

A relation between the two dimensionless pressures is

$$p^* = \frac{1}{\gamma M^2} p^+ \tag{8}$$

showing that in the low Mach regime, the two pressure references have a large difference of scale, proportional to M^2.

In the low Mach compressible regime on a bounded flow domain, it is usual, like for example in Bijl and Wesseling [8] or Jenny and Müller [26], to decompose the pressure $p = p(\mathbf{x}, t)$ into a mean thermodynamic pressure depending only on time $p_0(t)$ defined by

$$p_0(t) = \frac{1}{\text{vol}(\Omega)} \int_\Omega p(\mathbf{x}, t)\, \mathrm{d}V \tag{9}$$

and a hydrodynamic pressure fluctuation $p_2(\mathbf{x}, t)$, such that

$$p(\mathbf{x}, t) = p_0(t) + p_2(\mathbf{x}, t) \tag{10}$$

The mean pressure $p_0(t)$ is a background pressure, given by a global thermodynamic relationship. The reference thermodynamic pressure $p^{\text{t}}_{\text{ref}}$ scales the mean pressure $p_0(t)$, and the reference dynamical pressure $p^{\text{d}}_{\text{ref}}$ scales the fluctuation $p_2(\mathbf{x}, t)$. Therefore, by choosing the dynamical reference pressure $p^{\text{d}}_{\text{ref}}$, the dimensionless Euler equations and the thermodynamic state equation can be written in the same form as the dimensional ones:

$$\frac{\partial \rho^*}{\partial t^*} + \nabla^* \cdot (\rho^* \mathbf{u}^*) = 0 \tag{11a}$$

$$\frac{\partial \rho^* \mathbf{u}^*}{\partial t^*} + \nabla^* \cdot (\rho^* \mathbf{u}^* \otimes \mathbf{u}^*) + \nabla^* p^* = 0 \tag{11b}$$

$$\frac{\partial \rho^* e^*_t}{\partial t^*} + \nabla^* \cdot ((\rho^* e^*_t + p^*) \mathbf{u}^*) = 0 \tag{11c}$$

with

$$e^*_t = \frac{1}{(\gamma - 1)} \frac{p^*}{\rho^*} + \frac{1}{2} \mathbf{u}^{*2} \tag{12}$$

where $.^*$ denotes the dimensionless variables, given by $\rho = \rho_{\text{ref}} \rho^*$, $\mathbf{u} = u_{\text{ref}} \mathbf{u}^*$, $\mathbf{x} = L_{\text{ref}} \mathbf{x}^*$, $t = L_{\text{ref}} / u_{\text{ref}}\, t^*$.

The pressure decomposition gives

$$p^*(\mathbf{x}^*, t^*) = \frac{1}{\gamma M^2} p^+_0(t^*) + p^*_2(\mathbf{x}^*, t^*) \tag{13}$$

so that in the momentum equation $\nabla^* p^*$ can be rewritten as $\nabla^* p^*_2$. With this scaling, the Mach number M only appears explicitly in the pressure decomposition. A similar splitting can be applied to the total energy

$$\rho^* e^*_t(\mathbf{x}^*, t^*) = \frac{1}{(\gamma - 1)} \left(\frac{1}{\gamma M^2} p^+_0(t^*) + p^*_2(\mathbf{x}^*, t^*) \right) + \frac{1}{2} \rho^* \mathbf{u}^{*2}(\mathbf{x}^*, t^*) \tag{14}$$

leading to the definition:

$$\rho^* e^*_{t0}(t^*) = \frac{1}{(\gamma - 1)\gamma M^2} p^+_0(t^*) = \frac{1}{(\gamma - 1)} p^*_0(t^*) \tag{15a}$$

$$\rho^* e^*_{t2}(\mathbf{x}^*, t^*) = \frac{1}{(\gamma - 1)} p^*_2(\mathbf{x}^*, t^*) + \frac{1}{2} \rho^* \mathbf{u}^{*2}(\mathbf{x}^*, t^*) \tag{15b}$$

so that the energy conservation equation becomes

$$\frac{\partial \rho^* e^*_{t2}}{\partial t^*} + \nabla^* \cdot ((\rho^* e^*_{t2} + p^*_2) \mathbf{u}^*) + \frac{1}{(\gamma - 1) M^2} p^+_0(t^*) \nabla^* \cdot \mathbf{u}^* = - \frac{1}{(\gamma - 1)\gamma M^2} \frac{\partial p^+_0(t^*)}{\partial t^*} \tag{16}$$

and can be rewritten as

$$(\gamma-1)M^2\frac{1}{p_0^+(t^*)}\left[\frac{\partial\rho^* e_{t2}^*}{\partial t^*}+\nabla^*\cdot((\rho^* e_{t2}^*+p_2^*)\mathbf{u}^*)\right]+\nabla^*\cdot\mathbf{u}^*=-\frac{1}{\gamma}\frac{1}{p_0^+(t^*)}\frac{\partial p_0^+(t^*)}{\partial t^*} \tag{17}$$

This shows formally that in the zero Mach number limit, when the small scale fluctuations due to the acoustic waves are neglected (they would require additional reference scales to be taken into account), the energy equation ensures the divergence-free condition on the velocity field if the mean pressure is constant in time [41]. This dimensionless system is retained in the numerical methods analyzed in this study. In the numerical simulations, a decrease of the Mach number is therefore obtained by an increase of the mean thermodynamic pressure of the initial state p_0^*. For practical simulations of compressible flows, this scaling naturally arises every time a compressible simulation is initialized with an incompressible flow.

If the choice of the dynamical pressure as reference pressure is retained, dimensionless Euler equations are formally identical to the dimensional ones. The choice of the thermodynamic pressure based on the reference sound speed as reference pressure, on the contrary, introduces Mach number dependency in the Euler equations. The dimensionless Euler equations become:

$$\frac{\partial\rho^*}{\partial t^*}+\nabla^*\cdot(\rho^*\mathbf{u}^*)=0 \tag{18a}$$

$$\frac{\partial\rho^*\mathbf{u}^*}{\partial t^*}+\nabla^*\cdot(\rho^*\mathbf{u}^*\otimes\mathbf{u}^*)+\frac{1}{\gamma M^2}\nabla^* p^+=0 \tag{18b}$$

$$\frac{\partial\rho^* e_t^+}{\partial t^*}+\nabla^*\cdot((\rho^* e_t^+ + p^+)\mathbf{u}^*)=0 \tag{18c}$$

with

$$e_t^+=\frac{1}{(\gamma-1)}\frac{p^+}{\rho^*}+\frac{\gamma M^2}{2}\mathbf{u}^{*2} \tag{19}$$

and the same scaling for the pressure and the total energy

$$\rho^* e_t^*=\frac{1}{\gamma M^2}\rho^* e_t^+ \tag{20}$$

This scaling will be used to obtain an asymptotic analysis of the equations in the low Mach number limit.

In the following, we will only consider dimensionless variables and the superscript $.^*$ will be omitted for convenience.

3. Numerical methods

Euler equations for compressible flows form a hyperbolic system that can be written symbolically as

$$\frac{\partial W}{\partial t}+\nabla.\mathcal{F}(W)=0 \quad \text{in } \Omega \tag{21}$$

where $W=[\rho,\rho\mathbf{u},\rho e_t]^T$ is the conservative variable vector and $\mathcal{F}(W)$ is the Euler fluxes, homogeneous in W:

$$\mathcal{F}(W)=\mathcal{A}(W)W \quad \text{with } \mathcal{A}(W)=\frac{\partial\mathcal{F}}{\partial W} \tag{22}$$

Using a numerical approximation of the equations leads to a coupled system of differential equations for the discretized variables W^h:

$$\frac{dW^h}{dt}+\mathcal{K}^h(W^h)W^h=0 \tag{23}$$

Coupled time and space methods, developed on a Lax–Wendroff type approach, are beyond the scope of this study. These methods are very popular and efficient for scalar cases [24] but their high-order extension to Euler and Navier–Stokes equations is not trivial [18]. In this study, we restrict ourselves to separate time and space integrations, applying a multistage time integration for a given spatial scheme. As $\mathcal{K}^h(W^h)$ is a very large matrix of order $5N$ in 3D flows, N being the number of grid points, with a 5×5 block structure, explicit schemes are widely used to integrate the system (23). However explicit time-marching schemes are expensive at low Mach numbers because of a restrictive CFL stability condition based on the sound speed [16,9]. On the other hand, implicit schemes suffer from ill-conditioning when the Mach number goes to zero [17,46]. The explicit second-order-centered scheme is intrinsically unstable so that the resolution of the equation relies either on explicit upwind schemes, explicit high-order-centered schemes or at least implicit second-order schemes. Those classes of schemes are explored in this work starting from the widespread explicit upwind second-order Roe scheme. Its extension to a low Mach number regime is studied through the preconditioning technique of Turkel [55] adapted to unsteady compressible flows. Extensions to higher order spatial schemes are investigated by an explicit WENO-Roe scheme [27]. The WENO scheme is however well-known to be rather diffusive. In order to study the influence of the spatial dissipation

error, an explicit high-order-centered compact scheme [57] is also chosen. Both schemes are indeed usually retained for large-eddy simulation of unsteady compressible flows. The alternative choice of an implicit time integration is studied in association with a simple second-order-centered spatial scheme. In this study, the schemes are applied to the Euler case, but their extension to the Navier–Stokes equations is straightforward.

The methods are detailed in the following sections in their one-dimensional formulation, in order to simplify the presentation. Euler equations reduce to

$$\frac{\partial W}{\partial t}+\frac{\partial F}{\partial x}=0 \tag{24}$$

The Jacobian matrix of the Euler flux F of the conservative system is defined as $A=\partial F/\partial W$.

A general finite volume discretization of Eq. (24) leads to the following discrete equation:

$$\frac{\partial W_i}{\partial t}+\frac{F_{i+\frac{1}{2}}-F_{i-\frac{1}{2}}}{\Delta x}=0 \tag{25}$$

where W_i is the approximation solution at node i, and $F_{i+\frac{1}{2}}$ and $F_{i-\frac{1}{2}}$ the Euler fluxes at interfaces $i+\frac{1}{2}$ and $i-\frac{1}{2}$ around node i. The difference between the studied schemes rests in the time integration (explicit or implicit) and the flux reconstruction.

3.1. Explicit modified Roe–Turkel $\kappa-\alpha$ scheme

The Roe scheme is widely used for solving compressible flows. In this study, a second-order spatial accurate Roe–type scheme associated to a third-order MUSCL interpolation technique [33] is used to discretize the Euler fluxes. The numerical method is based on a cell-centered mixed finite volume/finite element discretization [19] for unstructured meshes. In addition, a preconditioning of the numerical dissipation for low Mach number flows is applied, following the work of Guillard and Viozat [23]. Their proposal allows an extension of explicit standard preconditioning techniques to unsteady flows [54,38]. For the preconditioned equations, the Euler fluxes at the interface $i+\frac{1}{2}$ of the finite volume cell around the node i are given by

$$F_{i+\frac{1}{2}}=\frac{1}{2}[F(W^-_{i+\frac{1}{2}})+F(W^+_{i+\frac{1}{2}})]-\alpha P^{-1}(\widetilde{W}_{i+\frac{1}{2}})|P(\widetilde{W}_{i+\frac{1}{2}})\widetilde{A}_{i+\frac{1}{2}}|(W^+_{i+\frac{1}{2}}-W^-_{i+\frac{1}{2}}) \tag{26}$$

where $\widetilde{A}_{i+\frac{1}{2}}$ is the Jacobian matrix evaluated at a state estimated with the Roe average [45], denoted here by $\{\tilde{\cdot}\}$. P is the Turkel preconditioner expressed in conservative variables [13]. In terms of entropy variables $U=[p,u,p/\rho^{\gamma}]^{\mathrm{T}}$, this preconditioner reads

$$P_U=\begin{bmatrix}\beta^2 & & \\ & 1 & \\ & & 1\end{bmatrix} \tag{27}$$

where β is a small coefficient of the order of the Mach number. $W^-_{i+\frac{1}{2}}$ and $W^+_{i+\frac{1}{2}}$ denote the MUSCL-FEM reconstruction of the conservative variables respectively at the inner- and outer-side of the finite volume cell around node i at interface $i+\frac{1}{2}$, as defined by

$$W^-_{i+\frac{1}{2}}=W_i+\frac{1}{2}(\nabla W)^-_{i+\frac{1}{2}}\cdot\vec{l}_i \tag{28a}$$

$$W^+_{i+\frac{1}{2}}=W_{i+1}-\frac{1}{2}(\nabla W)^+_{i+\frac{1}{2}}\cdot\vec{l}_i \tag{28b}$$

where $i+1$ belongs to the neighboring nodes of i, and the gradients at the inner- and outer-side of the interface are built by a linear combination of the centered gradient and the left and right gradients calculated respectively at the nodes i and $i+1$:

$$(\nabla W)^-_{i+\frac{1}{2}}\cdot\vec{l}_i=(1-\kappa)(\nabla W)^C_{i+\frac{1}{2}}\cdot\vec{l}_i+\kappa(\nabla W)^{\mathrm{L}}_i\cdot\vec{l}_i \tag{29a}$$

$$(\nabla W)^+_{i+\frac{1}{2}}\cdot\vec{l}_i=(1-\kappa)(\nabla W)^C_{i+\frac{1}{2}}\cdot\vec{l}_i+\kappa(\nabla W)^{\mathrm{R}}_{i+1}\cdot\vec{l}_i \tag{29b}$$

with $\vec{l}_i=\vec{x}_{i+1}-\vec{x}_i$, the distance vector between node i and its generic neighbor $i+1$. The gradient centered at edge $i+\frac{1}{2}$ is evaluated by

$$(\nabla W)^C_{i+\frac{1}{2}}\cdot\vec{l}_i=(W_{i+1}-W_i) \tag{30a}$$

whereas the left and right gradients are given by a combination of the nodal gradients and of the centered gradient at edge $i+\frac{1}{2}$:

$$(\nabla W)^{\mathrm{L}}_i\cdot\vec{l}_i=2(\nabla W)_i\cdot\vec{l}_i-(\nabla W)^C_{i+\frac{1}{2}}\cdot\vec{l}_i \tag{30b}$$

$$(\nabla W)^{\mathrm{R}}_{i+1}\cdot\vec{l}_i=2(\nabla W)_{i+1}\cdot\vec{l}_i-(\nabla W)^C_{i+\frac{1}{2}}\cdot\vec{l}_i \tag{30c}$$

The nodal gradient $(\nabla W)_i$ on node i (resp. $(\nabla W)_{i+1}$ on $i+1$) is obtained by averaging of the finite element gradients over the neighboring elements of the node. In this scheme, the numerical dissipation and dispersion are respectively controlled by the α and κ coefficients that have been set to $\alpha = 1/10$ and $\kappa = 1/3$ in order to minimize the errors of the spatial scheme, following the work of Carpentier [15] and Duchamp de Lageneste [21]. The standard second-order Roe scheme uses $\alpha = 1/2$. Time integration is carried out with the classical explicit fourth-order Runge–Kutta scheme which is conditionally stable under a CFL condition.

This explicit modified Roe–Turkel scheme has been applied to simulate unsteady compressible flows in complex geometries including the cases of high [21] and moderate [44,53] Mach numbers.

3.2. Explicit high-order upwind scheme

The class of high-order compressible upwind schemes is explored with a fifth order WENO-Roe scheme [27]. This scheme has been implemented for a cell-centered collocated discretization on structured curvilinear meshes. Derivatives of the contravariant components f of the Euler fluxes F are approached by a conservative difference

$$\left.\frac{\partial}{\partial\xi}[f(W)]\right|_i = \frac{1}{\Delta\xi}\left[f_{i+\frac{1}{2}} - f_{i-\frac{1}{2}}\right] \tag{31}$$

where $i+\frac{1}{2}$ and $i-\frac{1}{2}$ denote the cell interface. The flux is built at the cell interface by a WENO scheme applied to the projection $\bar{f}$ of the contravariant fluxes f on the characteristic lines, using the left eigenvector matrix evaluated at the interface with Roe-averaged values. The flux is upwinded according to the incoming or outgoing characteristics, or equivalently to the sign of the eigenvalues $\lambda_{i+\frac{1}{2}}$ of the Jacobian matrix at the interface. The following notation will be used

$$\text{if} \quad \lambda_{i+\frac{1}{2}} \geqslant 0 \quad \text{then } \bar{f}_{i+\frac{1}{2}} = \bar{f}^{+}_{i+\frac{1}{2}} \quad \text{and if} \quad \lambda_{i+\frac{1}{2}} < 0 \quad \text{then } \bar{f}_{i+\frac{1}{2}} = \bar{f}^{-}_{i+\frac{1}{2}} \tag{32}$$

where $\bar{f}^{+}_{i+\frac{1}{2}}$ and $\bar{f}^{-}_{i+\frac{1}{2}}$ are shifted respectively in the left and right direction with respect to the interface. The flux $\bar{f}_{i+\frac{1}{2}}$ is then transformed back to the physical space using the right eigenvector matrix at the interface. The WENO reconstruction of $\bar{f}^{+}_{i+\frac{1}{2}}$ and $\bar{f}^{-}_{i+\frac{1}{2}}$ is performed from k candidate stencils defined by

$$S_r(i) = \{x_{i-r}, \ldots, x_{i-r+k-1}\}, \quad r = 0, \ldots, k-1 \tag{33}$$

with $k = 3$ here. On each stencil $S_r(i)$, $(k-1)$th order polynomial interpolations of nodal fluxes are built

$$\bar{f}^{r-}_{i+\frac{1}{2}} = \sum_{n=0}^{k-1} c_{n,r+1}\bar{f}_{i+n+1+r+1-k} \tag{34a}$$

$$\bar{f}^{r+}_{i+\frac{1}{2}} = \sum_{n=0}^{k-1} c_{n,r}\bar{f}_{i+n+1+r-k} \tag{34b}$$

The weight coefficients $c_{n,r}$, for $n = 0, \ldots, k-1$ and $r = 0, \ldots, k$, are given in [27,14]. The WENO reconstruction is a convex combination of all the candidate stencils $\bar{f}^{r\pm}_{i+\frac{1}{2}}$, and is written as

$$\bar{f}^{\pm}_{i+\frac{1}{2}} = \sum_{r=0}^{k-1} \omega^{\pm}_r \bar{f}^{r\pm}_{i+\frac{1}{2}} \tag{35}$$

where

$$\omega^{\pm}_r = \frac{\alpha^{\pm}_r}{\sum_{n=0}^{k-1}\alpha^{\pm}_n} \quad \text{with } \alpha^{\pm}_r = \frac{d^{\pm}_r}{(\varepsilon + \beta^{\pm}_r(i))^2} \tag{36}$$

The constant $\varepsilon = 10^{-6}$ is chosen so that the denominator does not go to zero [50]. The functions $\beta^{\pm}_r(i)$ are regularity indicators of the stencil $S_r(i)$. They are calculated by undivided differences. The $d^{\pm}_r$ coefficients come from the chosen approximation on each stencil. Note that $d^{-}_r = d^{+}_{k-1-r}$ and $\beta^{-}_r(i) = \beta^{+}_r(i+1)$. Following the expressions proposed by Jiang and Shu [27], $d^{-}_0 = 3/10, d^{-}_1 = 6/10$ and $d^{-}_2 = 1/10$, and

$$\beta^{-}_0(i) = \frac{13}{12}(\bar{f}_{i-1} - 2\bar{f}_i + \bar{f}_{i+1})^2 + \frac{1}{4}(\bar{f}_{i-1} - 4\bar{f}_i + 3\bar{f}_{i+1})^2 \tag{37a}$$

$$\beta^{-}_1(i) = \frac{13}{12}(\bar{f}_i - 2\bar{f}_{i+1} + \bar{f}_{i+2})^2 + \frac{1}{4}(\bar{f}_i - \bar{f}_{i+2})^2 \tag{37b}$$

$$\beta^{-}_2(i) = \frac{13}{12}(\bar{f}_{i+1} - 2\bar{f}_{i+2} + \bar{f}_{i+3})^2 + \frac{1}{4}(3\bar{f}_i - 4\bar{f}_{i+1} + \bar{f}_{i+2})^2 \tag{37c}$$

This $k = 3$ WENO scheme allows a space resolution of order $2k-1 = 5$ in smooth areas to be obtained. Time integration is performed with the third-order TVD Runge Kutta method developed by Shu and Osher [51], without any adjustment to the low Mach number regime.

3.3. Explicit filtered high-order compact scheme

The class of explicit high-order-centered schemes is explored here with a five point compact Padé scheme [57], implemented on the cell-centered finite difference method on structured curvilinear meshes.

The gradient of the contravariant Euler fluxes f of F is obtained in each direction by the resolution of a tridiagonal system.

$$\alpha\left.\frac{\partial f}{\partial \xi}\right|_{i-1} + \left.\frac{\partial f}{\partial \xi}\right|_{i} + \alpha\left.\frac{\partial f}{\partial \xi}\right|_{i+1} = b\frac{f_{i+2}-f_{i-2}}{4\Delta\xi} + a\frac{f_{i+1}-f_{i-1}}{2\Delta\xi} \tag{38}$$

where α, a and b are constants. We used the fourth-order scheme corresponding to $\alpha = 1/4$, $a = 3/2$ and $b = 0$.

Centered compact difference schemes are non-dissipative and therefore cannot damp numerical instabilities due to high-frequency modes. When applied to compressible flows, a high-order filtering technique is usually applied to the spatial compact discretization to avoid spurious high-frequency oscillations. For any quantity f, the filtered value $\hat{f}$ is obtained by solving the following tridiagonal system

$$\alpha_f\hat{f}_{i-1} + \hat{f}_i + \alpha_f\hat{f}_{i+1} = \sum_{n=0}^{N}\frac{a_n}{2}(f_{i+n} - f_{i-n}) \tag{39}$$

giving an Nth-order scheme on a $2N+1$ stencil. Parameter α_f satisfies $-0.5 < \alpha_f \leqslant 0.5$ where higher values correspond to a less dissipative filter. The sixth-order filter proposed by Visbal and Gaitonde [58] is retained here, where the coefficients are defined by $a_0 = \frac{11}{16} + \frac{5}{8}\alpha_f, a_1 = \frac{15}{32} + \frac{17}{16}\alpha_f, a_2 = \frac{-3}{16} + \frac{3}{8}\alpha_f, a_3 = \frac{1}{32} - \frac{1}{16}\alpha_f$ and $a_4 = 0$, with $\alpha_f = 0.49$ in order to minimize the dissipation effect.

Time integration is carried out with the third-order TVD Runge Kutta method [51]. As for the WENO scheme, no low Mach number modification is performed.

3.4. Implicit centered scheme

To illustrate the class of implicit centered schemes, a second-order-centered formulation of the Euler fluxes has been implemented on a cell-centered unstructured finite volume discretization. The numerical flux at the cell interface $F_{i+\frac{1}{2}}$ is interpolated with a centered second-order method:

$$F_{i+\frac{1}{2}} = \frac{1}{2}A(\widetilde{W}_{i+1} + \widetilde{W}_i) \quad \text{with } \widetilde{W}_i = W_i + \frac{\Delta x}{2}(\nabla W)_i^C \tag{40}$$

where A is the Jacobian matrix of Euler flux and $(\nabla W)_i^C$ is the centered gradient evaluated on the cell around node i using the Green theorem.

The Euler equations are integrated in time with a second-order implicit Backward Differentiation Formula (BDF) scheme

$$\frac{3W_i^{n+1} - 4W_i^n + W_i^{n-1}}{2\Delta t} + \frac{1}{\Delta x}(F(W)_{i+\frac{1}{2}}^{n+1} - F(W)_{i-\frac{1}{2}}^{n+1}) = 0 \tag{41}$$

The nonlinear system in W^{n+1}, symbolically denoted as $G(W^{n+1}) = 0$, is solved by an iterative Newton method:

$$\left(\frac{\partial G(W^{n+1,k})}{\partial W^{n+1}}\right)(W^{n+1,k+1} - W^{n+1,k}) = -G(W^{n+1,k}) \tag{42}$$

The Jacobian of this system, $J = \partial G/\partial W$ is expressed in terms of the Jacobian matrix of the Euler fluxes A. In order to simplify the evaluation of the Jacobian J, the Jacobian matrix A is calculated with a first order linearization. The linear system is solved by a GMRES method, with a block Jacobi preconditioning, from the PETSC library [5]. The resulting scheme is of the second-order in time and space. It is linearly unconditionally stable.

In the low Mach number regime, the linear system becomes difficult to solve, due to the large difference between the magnitude of the total energy and the pressure, with both a leading order of $O(M^{-2})$, and that of the density and the velocity of leading order O(1), following the chosen dimensionless system. This can be corrected with the pressure decomposition presented in Section 2. Such a decomposition has been applied to low Mach numbers flows by Shuen [52], Bijl and Wesseling [8] or Van der Heul et al. [56]. This approach attenuates the cancellation problem due to round-off errors occurring because of the large difference between the order of the variables and their low Mach number fluctuations [49]. The linear system being solved iteratively, this prevents the convergence of the solution degenerating when the Mach number decreases. Moreover, this approach is suitable for long time integration of unsteady flows and is therefore interesting in a LES/DNS perspective.

3.5. Spectral error analysis of the numerical schemes

The spatial and temporal discretization errors of the different schemes are evaluated in the case of the one-dimensional linear advection equation on a regular mesh of size h. Using standard Fourier analysis (see e.g. [43]), dissipation and

dispersion errors are evaluated respectively as the error in amplitude and phase for the propagating wave solution of wavenumber k. Errors are plotted versus the cell wavenumber kh in Fig. 1, for CFL = 0.6. For large kh, the least dissipative scheme is the implicit centered scheme but the PADE scheme is more accurate for the resolvable scales (i.e. $kh \leqslant 1$). The PADE scheme has also the lowest dispersive error. It should be pointed out that the finite volume second-order schemes are relatively accurate as compared to the high-order finite difference schemes and especially much more precise than the standard second-order finite difference scheme. The two centered schemes (implicit centered scheme and compact PADE scheme) are less dissipative than the two Roe upwind schemes and the two high-order schemes (PADE and WENO) have less dispersion error than the two second-order schemes. However this analysis does not take into account the low Mach number preconditioning for the Roe–Turkel scheme, nor the high wavenumber filtering for the PADE scheme.

4. Asymptotic analysis of model flow

4.1. Model flow

The plane Taylor vortex selected for the comparison of the numerical methods is defined at initial time $t = 0$ in terms of the dimensionless variables introduced in Section 2 by

$$\rho(\mathbf{x},0) = \rho_0 = 1 \tag{43a}$$

$$\mathbf{u}(\mathbf{x},0) = \mathbf{u}_0(\mathbf{x}) = \left(\frac{\partial\psi_0}{\partial y}, -\frac{\partial\psi_0}{\partial x}\right) \quad \text{with } \psi_0 = \frac{1}{\pi}\sin(\pi x)\sin(\pi y) \tag{43b}$$

$$p(\mathbf{x},0) = p_0 + \frac{1}{4}(\cos(2\pi x) + \cos(2\pi y)) \tag{43c}$$

with $p_0 = 1/\gamma M^2$. This flow evolves inside the square domain $[0,1] \times [0,1]$ of the (x,y) plane and is subjected to the zero normal velocity condition on the boundaries. In the simulations, the variations of the Mach number are set by the value of p_0 in the initial flow field. In order to simplify the asymptotic analysis, the ratio p/p_0 will be defined hereafter as $P \equiv p/p_0$, and be written as

$$P(\mathbf{x},0) = P_0 + \gamma M^2 P_2(\mathbf{x}) \quad \text{with } P_0 = 1 \quad \text{and} \quad P_2(\mathbf{x}) = \frac{1}{4}(\cos(2\pi x) + \cos(2\pi y)) \tag{44}$$

The initial velocity field has zero divergence and can be described as a vortex rotating anticlockwise around the center of the unit box. Each streamline has its own period of rotation $T(\psi_0)$ increasing from $T(1/\pi) = 2$ for the circular streamlines close to the center of the domain and going up to $T(0) = \infty$ for the streamlines near the boundaries, because of the existence of hyperbolic stagnation points at the corners. The initial flow is a steady solution of the incompressible Euler equations. With respect to the compressible Euler equations, this flow is no longer constant in time. Time and space fluctuations of all variables are produced with a dependency on the Mach number value. These fluctuations occur at different time scales. One part of the motion is associated to the convective time of the vortex and is explained by the fact that streamlines in the initial flow are not lines of constant entropy. At $t = 0$, since density is uniform, entropy varies throughout the flow with an amplitude which is $O(M^2)$ in the zero Mach number limit, just like pressure P. Because of entropy conservation, these variations are advected along the streamlines, thereby generating $O(M^2)$ fluctuations of density. Concomitantly, a response is generated on a short

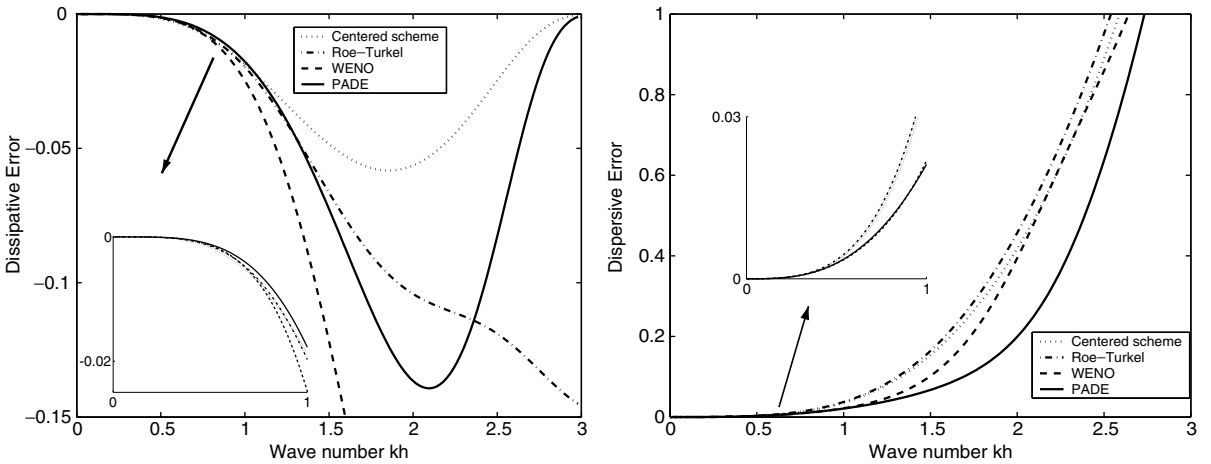

(a) Dissipative error at $CFL = 0.6$ (b) Dispersive error at $CFL = 0.6$

Fig. 1. Spectral error analysis for the 1D linear advection equation.

time scale. The fact that the material derivative of the density has non-zero values means that the velocity field cannot remain solenoidal, because of mass conservation. Because of the divergence-free conditions at $t = 0$, the flow develops compressible velocity fluctuations of order $O(M^2)$, evolving on the acoustic time scale $\tau = t/M$. This motion generates $O(M^3)$ fluctuations in the density and the pressure fields.

4.2. Expansion around zero Mach number limit

In order to compare the different numerical methods, an approximation of the solution is sought as an asymptotic expansion in powers of the Mach number. Fluid dynamics is the field of numerous applications of the method of asymptotic expansions. One can refer to Zeytounian [61,62] for a detailed exposition of this question. Zank and Mattheus [60] also discuss physical aspects of the different models of the incompressible limit of the Navier–Stokes equations. In the context of low Mach numbers flows, Klein [31] presents applications of asymptotic expansions to the development of numerical methods. Certain technical aspects are presented by Meister [36] and Ali [3]. More insights into the mathematical nature of the problem and a list of open questions are given in Schochet [48]. Proof of the convergence of asymptotic expansions can be found in Klainermann and Majda [30] and in Schochet [47].

The asymptotic expansion is sought starting from the mass, momentum and, for the sake of simplicity, the entropy equation which is used instead of that of energy. This equation reads

$$\frac{\partial s}{\partial t} + \mathbf{u} \cdot \nabla s = 0 \tag{45}$$

with $s = c_v \ln(P/\rho^\gamma)$, following the perfect gases law, where c_v is the constant volume heat capacity. The vector of variables $[P, \mathbf{u}, s]$ is sought as a two-time scale expansion in powers of Mach number as

$$[P, \mathbf{u}, s] = [P_0, \mathbf{u}_0, s_0](\mathbf{x}, \tau, t) + \sum_{n \geqslant 1} M^n [\gamma P_n, \mathbf{u}_n, s_n](\mathbf{x}, \tau, t) \tag{46}$$

in which the time dependence of the coefficients is expressed in function of both the rapid time $\tau = t/M$ and the slow time t. Introducing these expansions into the governing equations and collecting the terms that appear at the different powers of M yields the following hierarchy of equations

$$\begin{aligned} &\nabla P_0 = \frac{\partial P_0}{\partial \tau} = 0 \\ &\frac{\partial \mathbf{X}_n}{\partial \tau} + \mathbb{L}\mathbf{X}_n = \mathbf{f}_n \quad n = 0, 1, 2, \ldots \end{aligned} \tag{47}$$

where $\mathbf{X}_n = [P_{n+1}, \mathbf{u}_n, s_n]$ and $\mathbb{L}$ is the differential operator

$$\mathbb{L} = \begin{pmatrix} 0 & \gamma P_0 \nabla . & 0 \\ \rho(P_0, s_0)^{-1} \nabla & 0 & 0 \\ 0 & 0 & 0 \end{pmatrix} \tag{48}$$

The right-hand side $\mathbf{f}_n$ is such that $\mathbf{f}_0 = 0$ and, for $n \geqslant 1$, $\mathbf{f}_n$ is a function of

$$\frac{\partial \mathbf{X}_{n-1}}{\partial t}, \left[\nabla \mathbf{X}_m, \mathbf{X}_m, \frac{\partial \mathbf{X}_m}{\partial \tau}, m = 1, \ldots, n-1 \right], s_n \tag{49}$$

To make the system (47) solvable, a particular property is used to express the first term in the list, since the derivatives with respect to the slow time are still unknown at this stage of the procedure. This condition states that variations of all the variables must be at most linear functions of the rapid time [48,36]:

$$\lim_{\tau \to \infty} \frac{\mathbf{X}_n(\mathbf{x}, \tau, t)}{\tau} = 0 \quad \text{for } n \geqslant 0 \tag{50}$$

This condition, usually called the sublinearity condition, is a sufficient condition for the asymptotic expansion to be uniformly valid in time. In the following, all variables will be assumed to be decomposed in a slow part, defined as the average over the rapid time scale

$$\overline{\mathbf{X}}_n(\mathbf{x}, t) = \lim_{\tau \to \infty} \frac{1}{\tau} \int_0^\tau \mathbf{X}_n(\mathbf{x}, \tau', t) \, \mathrm{d}\tau' \tag{51}$$

and in a rapid part, defined by the difference

$$\delta \mathbf{X}_n(\mathbf{x}, \tau, t) = \mathbf{X}_n(\mathbf{x}, \tau, t) - \overline{\mathbf{X}}_n(\mathbf{x}, t) \tag{52}$$

A particular case, leading to an important simplification of the system (47), is when the initial variations of ∇s are at most $O(M)$. In that case, and if the total volume of the flow does not vary, s_0 and P_0 remain constant and the left-hand side is a linear differential operator with constant coefficients. In the present study, $\nabla s = O(M^2)$, so that this property is naturally

satisfied. Applying the decomposition in slow and rapid parts to the system (47), two sets of equations are obtained, one by averaging with respect to the rapid time and another, by subtracting the averaged equations from the original ones. The latter form a system for the fluctuations on the rapid time τ

$$\frac{\partial \delta \mathbf{X}_n}{\partial \tau} + \mathbb{L}\delta \mathbf{X}_n = \delta \mathbf{f}_n = \mathbf{f}_n - \bar{\mathbf{f}}_n \quad n = 0, 1, 2, \ldots \tag{53}$$

in which the slow time appears as a parameter. The left-hand side is the differential operator of the linear acoustics. As said earlier, conditions have to be imposed onto the right-hand side of the system in order to satisfy the sublinearity property. For a given n, the condition takes the form of an equation for the derivative of $\delta \mathbf{X}_{n-1}$ with respect to the slow time t. For our model flow, the acoustic operator $\mathbb{L}$ has constant coefficients and the general solution of the associated homogeneous system is such that

$$\delta P_n(\mathbf{x}, \tau, t) = \sum_{p,q} C_{n,pq} \cos(p\pi x) \cos(q\pi y) \cos(2\pi f_{pq} \tau + \varphi_{n,pq}) \tag{54}$$

with $f_{pq} = \frac{1}{2}\sqrt{p^2 + q^2}\sqrt{P_0/\rho_0}$.

Taking into account the particular initial conditions of our model flow, the low Mach number expansion takes the following form

$$\mathbf{u}(\mathbf{x}, t) = \mathbf{u}_0(\mathbf{x}) + M^2[\bar{\mathbf{u}}_2(\mathbf{x}, t) + \delta \mathbf{u}_2(\mathbf{x}, \tau, 0)] + M^3 \delta \mathbf{u}_3(\mathbf{x}, \tau, t) + \cdots \tag{55a}$$

$$P(\mathbf{x}, t) = 1 + \gamma M^2 P_2(\mathbf{x}) + \gamma M^3 \delta P_3(\mathbf{x}, \tau, 0) + \gamma M^4[\bar{P}_4(\mathbf{x}, t) + \delta P_4(\mathbf{x}, \tau, t)] + \cdots \tag{55b}$$

$$s(\mathbf{x}, t) = M^2 \bar{s}_2(\mathbf{x}, t) + M^4 \bar{s}_4(\mathbf{x}, t) + \cdots \tag{55c}$$

and for density the expansion reads

$$\rho(\mathbf{x}, t) = 1 + M^2 \bar{\rho}_2(\mathbf{x}, t) + M^3 \delta \rho_3(\mathbf{x}, \tau, 0) + M^4[\bar{\rho}_4(\mathbf{x}, t) + \delta \rho_4(\mathbf{x}, \tau, t)] + \cdots \tag{55d}$$

The first two non-trivial equations for the averaged variables are the equations of $\bar{\mathbf{u}}_2$ and $\bar{s}_2$. The equation of $\bar{s}_2$ is the transport equation by the basic flow

$$\frac{\partial \bar{s}_2}{\partial t} + \mathbf{u}_0 \cdot \nabla \bar{s}_2 = 0 \tag{56}$$

The initial variations of entropy are thus convected by the basic flow. This effect induces density variations at order $n = 2$ which are governed by the following equation

$$\frac{\partial \bar{\rho}_2}{\partial t} + \mathbf{u}_0 \cdot \nabla \bar{\rho}_2 = \mathbf{u}_0 \cdot \nabla P_2 = -\nabla \cdot \bar{\mathbf{u}}_2 = -\frac{1}{2}\mathbf{u}_0 \cdot \nabla(\mathbf{u}_0^2) \tag{57}$$

The equality between the last two terms shows that a compressible, steady contribution appears in the velocity field at order $n = 2$.

The first non-zero coefficients for the rapid time variations are obtained at order $n = 2$. For $t = 0$, the solution of (53) is found using the initial conditions

$$\nabla \cdot \delta \mathbf{u}_2(\mathbf{x}, 0, 0) = -\nabla \cdot \bar{\mathbf{u}}_2(\mathbf{x}, 0) = \mathbf{u}_0 \cdot \nabla P_2 \tag{58a}$$

$$\nabla \delta P_3(\mathbf{x}, 0, 0) = 0 \tag{58b}$$

At this order, the expression on the right-hand side of (53) vanishes and $(\delta P_3, \delta \mathbf{u}_2)$ is found as the sum of the two particular eigenmodes $(p,q) = (3,1), (1,3)$ oscillating at frequency $f_{31} = f_{13} = \sqrt{10}/2$:

$$\delta P_3(\mathbf{x}, \tau, 0) = \frac{1}{4\sqrt{10}} \sin\left(\sqrt{10}\pi\tau\right)(\cos \pi x \cos 3\pi y - \cos 3\pi x \cos \pi y) \tag{59a}$$

$$\delta \mathbf{u}_2(\mathbf{x}, \tau, 0) = \frac{1}{40} \cos\left(\sqrt{10}\pi\tau\right) \begin{vmatrix} 3 \sin 3\pi x \cos \pi y - \sin \pi x \cos 3\pi y \\ \cos 3\pi x \sin \pi y - 3 \cos \pi x \sin 3\pi y \end{vmatrix} \tag{59b}$$

At the next order $n = 3$, the right-hand side of (53), which can be made explicit by substitution of (59a–b), represents a source term oscillating on the rapid time. The general solution is the sum of a linear combination of the acoustic eigenmodes and of terms corresponding to the forced response. For the pressure, the solution is given by

$$\delta P_4(\mathbf{x}, \tau, 0) = \sum_{p,q} \left(A_{4,pq} \cos(\sqrt{10}\pi\tau) + B_{4,pq} \cos(2\pi f_{pq}\tau)\right) \cos(p\pi x) \cos(q\pi y) \tag{60}$$

and the different coefficients and frequencies are reported in Table 1.

We note that for the lowest orders, the sublinearity condition implies that $\delta \mathbf{X}_n$ does not depend on t, for $n = 0, 1, 2$. In particular, the amplitudes of δP_3 and $\delta \mathbf{u}_2$ remain equal to their initial value at $t = 0$. At higher orders, the fluctuating quantities can depend on the slow time. As an example, in δP_4, contributions of the $(1,3)$ and $(3,1)$ modes, which are zero at initial time, have to be taken into account when $t > 0$ as functions of the slow time. The equation of their amplitude involves a coupling with $s_2(\mathbf{x}, t)$ and can be obtained from the sublinearity condition for $(\delta P_5, \delta \mathbf{u}_4)$.

Table 1
Coefficients in expression of $\delta P_4(\mathbf{x},\tau,t=0)$

(p,q)	(2,2)	(4,0); (0,4)	(2,0); (0,2)	(2,4); (4,2)
f_{pq}	$\sqrt{2}$	2	1	$\sqrt{5}$
$A_{4,pq}$	2/5	1/10	1/40	7/200
$B_{4,pq}$	−7/16	−5/64	−1/32	−19/800

With the perspective of comparison with the numerical simulations, the slow time solution will be explored through the $\bar{\rho}_2(\mathbf{x},t)$ term and the fast time contribution will be analyzed with the acoustic term. Their behavior according to the asymptotic expansion is illustrated in the next two sections.

4.3. Slow time solution

The solution of (57) is given by

$$\bar{\rho}_2(\mathbf{x},t) = [P_2(\mathbf{x}) - P_2(\mathbf{x_0}(\mathbf{x},t))] \tag{61}$$

where $\mathbf{x}_0(\mathbf{x},t)$ is the initial position of a particle moving with the velocity field $\mathbf{u}_0$ and located at $\mathbf{x}$ at time t. Using (43b), (44) and the change of variables $\theta = \arcsin(m^{-1/2}\cos(\pi x))$, $\phi = \arcsin(m^{-1/2}\cos(\pi y))$, the solution can be expressed in terms of the first order elliptic integral $F(\alpha|m)$ of parameter $m = 1-\pi^2\psi_0^2 = 1-\sin^2(\pi x)\sin^2(\pi y)$ and of the associated Jacobi's elliptic function sn [1]. This solution reads

$$\bar{\rho}_2(\mathbf{x},t) = \frac{m}{2}[\sin^2\theta + \sin^2\phi - \mathrm{sn}^2(F(\theta|m) + (\mathrm{sgn}\phi)\pi t) - \mathrm{sn}^2(F(\phi|m) - (\mathrm{sgn}\theta)\pi t)] \tag{62}$$

and is evaluated numerically by using Matlab integration procedures.[1] Variations of $\bar{\rho}_2(\mathbf{x},t)$ are illustrated in Fig. 2 at different times. Since density is constant initially, the convection term in (57) has a negligible effect at the first values of time. Accordingly, the symmetric pattern observed at $t = 0.1$ is still similar to the isolevels of the source term. The sequence of images shows that this pattern is continuously stretched and convected along the streamlines, leading to the particular lamellar structure which develops at the large time values. As mentioned earlier, $t = 2.0$ is the rotation period of the fluid particles near to the vortex center. This particular value of time will be retained for the later comparison of the numerical schemes. The final value of time $t = 8.8$ corresponds to a little more than four rotation periods of the vortex center. The sequence of Fig. 2 shows that the finer oscillations of $\bar{\rho}_2$ are located near the boundaries and that their length scale decreases as time evolves. A cross-section in the $\bar{\rho}_2$ field at $t = 8.8$ along a diagonal of the domain is plotted in Fig. 3 where the fine structures located in the corners of the domain can be seen. In the whole domain, the finer structures are found near the walls at the mid-domain vertical or horizontal sections. At $t = 8.8$, their size is half the size of the finer structures of the corners. This spatial distribution has determined the choice of an admissible coarse mesh size for the numerical simulations, as detailed in Section 5.

When observed at a fixed location, the time evolution of $\bar{\rho}_2$ is periodic with a period equal to $T(\psi_0)/4$, thus depending on the value of the stream function. Fig. 4 shows the time history of $\bar{\rho}_2$ at a point close to the middle of the bottom wall. At this location, the simulations are expected to be very sensitive to the capacity of the methods to capture the high-frequency spatial oscillations and hence gives an indication about the influence of the spatial numerical dissipation. Low Mach number variations of density are of the order of $O(M^2)$ so that the ability of the methods to exhibit the correct similitude in Mach number can be evaluated by comparing of the time evolutions of $\bar{\rho}_2$.

4.4. Fast time solution

The low Mach number expansion of the pressure shows that the leading term for the acoustic pressure is $\gamma\delta P_3(\mathbf{x},\tau,0)M^3$. This term corresponds to the (1,3) and (3,1) eigenmodes of the acoustic operator and oscillates on rapid time τ as $\sin(\sqrt{10}\pi\tau)$. The fourth-order term is the sum of a contribution $\overline{P}_4(\mathbf{x},t)$, evolving on the slow time scale, and an acoustic fluctuation $\delta P_4(\mathbf{x},\tau,t)$. The time evolution of $\delta P_4(\mathbf{x},\tau,t)$ oscillates on the rapid time scale, as given by Eq. (60), with the primary frequency $f_{13} = f_{31} = \sqrt{10}/2$ (that of δP_3) and with four additional frequencies, associated to four couples of additional eigenmodes. Frequencies and amplitudes of the corresponding oscillations are given in Table 1 near to $t = 0$. fourth-order terms of the development have a small influence on the acoustic pressure for very low Mach numbers. However, for higher Mach number values, such as $M = 0.1$, they cannot be entirely neglected. The asymptotic fast time solution will therefore be characterized by the following acoustic pressure

$$\mathcal{P}_3^{\mathrm{as}}(\mathbf{x},\tau,t) \equiv \delta P_3(\mathbf{x},\tau,0) + M[\overline{P}_4(\mathbf{x},0) + \delta P_4(\mathbf{x},\tau,0)] \tag{63}$$

Much attention will be paid to the two following benchmarks. The first one addresses the evolution of pressure fluctuation on short time near the origin and the presence of the additional frequencies in the signal. The second considers the long time behavior of the oscillation amplitude at the primary frequency.

[1] The Matlab code is available on request to the authors.

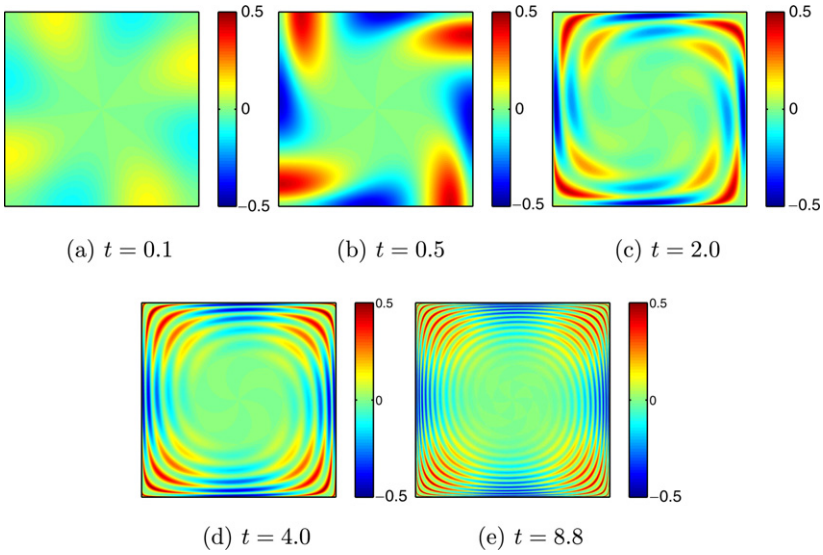

Fig. 2. $\bar{\rho}_2(x, y, t)$ at different times.

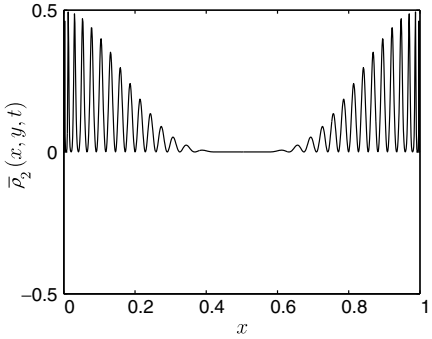

Fig. 3. $\bar{\rho}_2(x, y, t)$ profile at $t = 8.8$ on the diagonal line $x = 1 - y$.

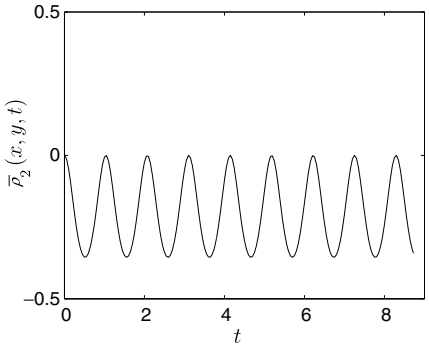

Fig. 4. Time evolution of $\bar{\rho}_2(x, y, t)$ at ($x = 0.5$, $y = 0.05$) with t.

To compare different Mach numbers, the evolution of the pressure fluctuation has to be analyzed in term of the rapid time scale. Fig. 5a shows $\mathcal{P}_3^{as}(\mathbf{x}, \tau, t)$ on the interval $0 < \tau < 5$. For $M = 0.1$ the upper value of τ corresponds to $t = 0.5$, a quarter rotation of the vortex core, whereas, for $M = 0.01$, the same value corresponds to $t = 0.05$. The τ interval corresponds approximately to *8* periods of the oscillation of the third-order acoustic part. The influence of the fourth-order terms on $\mathcal{P}_3^{as}(\mathbf{x}, \tau, t)$ is not visible at $M = 0.01$, their amplitude being ten times smaller than at $M = 0.1$. The corresponding additional frequencies can be extracted by a Fourier transform of the signal.

To analyze the amplitude of the primary oscillation on the long time, the very large number of acoustic periods makes it more convenient to represent the signal by its envelope. The procedure is first to filter out the extra frequencies, those com-

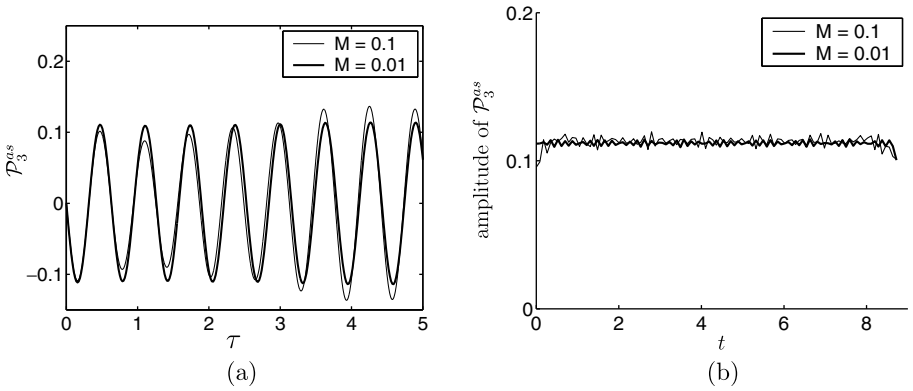

Fig. 5. Asymptotic solution $\mathcal{P}_3^{as} \equiv \delta P_3(\mathbf{x},\tau,0) + M[\overline{P}_4(\mathbf{x},0) + \delta P_4(\mathbf{x},\tau,0)]$ (acoustic pressure) at ($x = 0.66$, $y = 0.05$): (a) time evolution with τ, (b) time evolution of the amplitude of $\delta P_3(\mathbf{x},\tau,0)$ with t after removing from $\mathcal{P}_3^{as}$ the additional frequencies arising at the fourth-order of the Mach expansion.

ing from the fourth-order term, by using a Fourier band-pass filter around the frequency $f_{31} = f_{13}$ of the $\delta P_3(\mathbf{x},\tau,0)$ term and secondly to apply a Hilbert transform to the output, in order to obtain the time variation of the amplitude of the oscillation. Fig. 5b shows that, by following this procedure, it is possible to verify that the amplitude of $\mathcal{P}_3^{as}(\mathbf{x},\tau,t)$ is constant, except for small wiggles, which are more pronounced at $M = 0.1$ than at $M = 0.01$, due to the fact that the frequencies to be filtered are not clearly separate from the sideband of the primary frequency. Despite this artifact, the solution is shown to be constant and practically Mach number independent.

5. Numerical simulations

The numerical schemes presented in Section 3 are now compared with regard to their ability to capture the time evolution of the plane inviscid vortex at low Mach numbers.

The flow is initialized as given in Eq. (43a–b–c), and a slip wall condition is applied on the unit box boundaries, so that every scheme verifies $\mathbf{u}\cdot\mathbf{n} = 0$ where $\mathbf{n}$ is the wall normal unit vector. For upwind schemes, the outgoing pressure wave is determined using the characteristics whereas, for the centered scheme, a zero pressure wall normal derivative is used. This allows to build the Euler fluxes on the walls and ensures that their contribution is entirely due to the normal constraint imposed by the pressure at boundaries.

The numerical solutions are compared to the asymptotic solution for the two Mach number values: $M = 0.1$ and $M = 0.01$. Simulations are performed up to $t = 8.8$ corresponding to a little more than four rotation periods of the vortex core. Comparisons with the asymptotic solution are performed on a regular mesh of the (x,y) plane of 120×120 nodes. This mesh size allows the different schemes to reasonably predict the properties of the flow while exhibiting substantial differences for long time integration. If the mesh cell is able to describe the density fluctuations in the corners of the domain at $t = 8.8$, it is about two times too large to predict the highest spatial frequencies of the slow part of the density occurring near the middle of the walls. Unless specified, time integration satisfies the same CFL constraint for all the methods, taking CFL = 0.6, at $M = 0.1$ and $M = 0.01$, regardless of the low Mach number treatment. The convergence criteria of Newton's method, which are the same for all implicit simulations, are such that the solution of the nonlinear system is found when the nonlinear residuals have decreased by six orders of magnitude within a maximum of 50 iterations. At each nonlinear step, the linear system is solved within a maximum of 500 iterations and the solution converges when the residual has decayed by 9 orders. With those criteria, on the 120×120 mesh and at CFL = 0.6, the Newton method requires about 4 (resp. 16) iterations whereas the linear system is solved after 3 (resp. 12) iterations at $M = 0.1$ (resp. 0.01). The accuracy of the selected methods is discussed in Section 5.1. The slow and rapid parts of the low Mach number flow predicted by the simulations are analyzed in Sections 5.2 and 5.3 respectively. The influence of the low Mach number treatment is given in Section 5.4 together with a discussion about the convergence criteria of the implicit solver.

5.1. Accuracy of the numerical methods

The compressible solutions $\mathbf{u}(\mathbf{x},t)$ predicted by the numerical schemes are compared at $t = 8.8$ to the incompressible initial solution $\mathbf{u}_0(\mathbf{x})$, corresponding to the zero-order term in the low Mach number asymptotic development, for $M = 0.1$ and $M = 0.01$. The evolution of the L_2 norm of the error $\|\mathbf{u} - \mathbf{u}_0\|_2$ with the mesh refinement is shown in Fig. 6 for every scheme. The second and fourth-order slopes have been added to facilitate comparison.

The centered scheme (Fig. 6a) exhibits the lowest error level on the coarser mesh of all schemes, showing that the method has here the lowest numerical dissipation level. The global second-order accuracy of the centered method is well recovered for both Mach number flows. Moreover, the error level is the same for both Mach number values, showing that the global

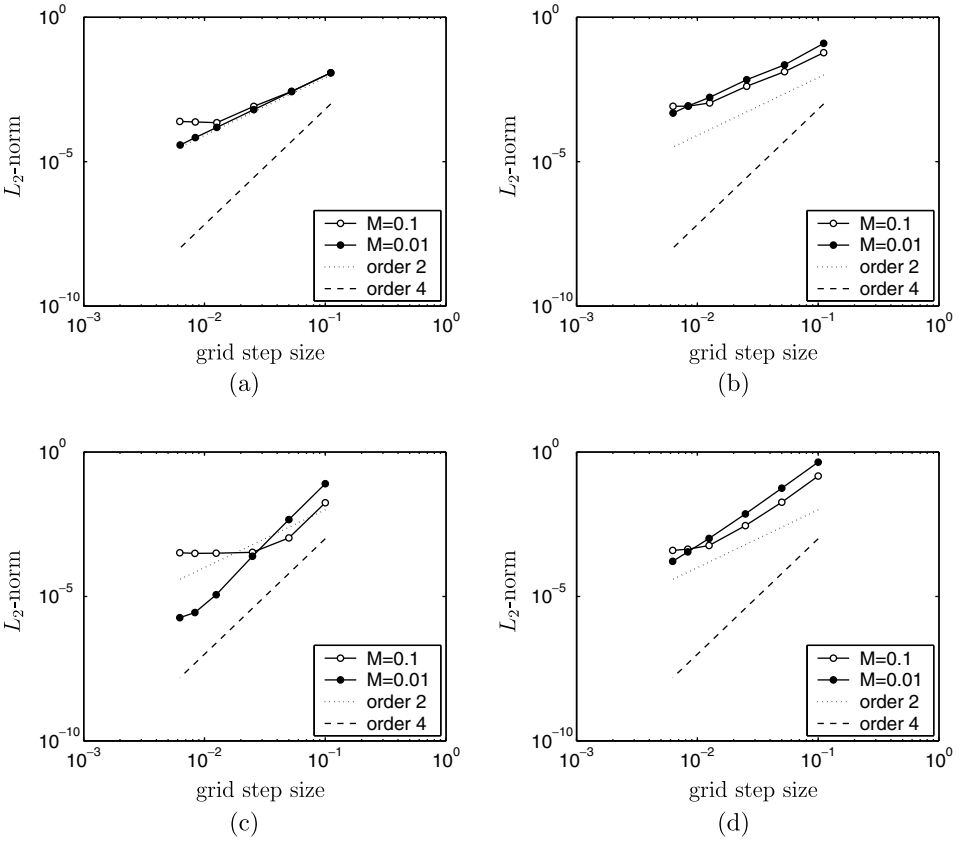

Fig. 6. Norm L_2 of the velocity error between the compressible and incompressible solutions: (a) implicit centered scheme, (b) Roe–Turkel scheme, (c) fourth-order PADE scheme, (d) fifth-order WENO scheme.

accuracy is Mach number independent. The high-order terms of the Mach number expansion have a growing influence on the compressible solution for higher Mach number flows, at $M = 0.1$. This is the reason why the difference between the compressible solution and the zero Mach number expansion term saturates for the finer meshes where the solution is more accurately predicted. It should be noted that a saturation level at $M = 0.1$ exists and is identical ($\sim 10^{-4}$) for every scheme, but is reached more or less rapidly depending on the global numerical dissipation error and the accuracy of the scheme. For the $M = 0.01$ case, the saturation level, linked to the higher order terms of the Mach number development, is therefore lower, and the centered scheme does not reach it yet on the finer mesh.

The second-order accuracy of the Roe–Turkel method is correctly recovered as well (see Fig. 6b), with a higher global error level than that obtained by the centered scheme. The same general behavior is observed between both second-order schemes. However, a slightly higher error level at $M = 0.01$ than at $M = 0.1$ indicates that the Roe–Turkel scheme is not entirely Mach independent. The numerical dissipation is indeed not identical at $M = 0.1$ and $M = 0.01$.

The high-order compressible PADE and WENO schemes (Figs. 6c and d) do exhibit a large difference between the error level at $M = 0.01$ and $M = 0.1$, that can be explained by the absence of Mach number preconditioning in these methods. At $M = 0.1$, the error level of the WENO scheme on the coarser mesh is very close to that of the Roe–Turkel scheme, whereas the PADE scheme error level is closer to the second-order-centered implicit scheme. The fourth-order accuracy of the PADE scheme is well captured for both Mach numbers even if the saturation level is very rapidly reached for $M = 0.1$. Because of its high-order discretization error, the saturation level ($\sim 10^{-6}$) is also reached for the finer meshes for $M = 0.01$. The difference between the two levels varies like M^2, as expected by the asymptotic analysis of the velocity field. The global accuracy of the WENO scheme is close to 3.5. This scheme is indeed of the third-order close to the boundaries and of the fifth order away from them. Taking into account that the scheme molecule requires six points per direction, the influence of the boundaries is not negligible on the coarse meshes.

5.2. Numerical prediction of the slow time part

From the numerical solutions, the second-order truncation of the density field, defined as

$$\mathcal{R}_2(\mathbf{x}, t) \equiv \frac{1}{M^2}[\rho(\mathbf{x}, t) - 1] \tag{64}$$

is computed and compared to the value of

$$\mathcal{R}_2^{\mathrm{as}}(\mathbf{x},t) \equiv \bar{\rho}_2(\mathbf{x},t) \tag{65}$$

obtained from the asymptotic solution. Isovalues of $\mathcal{R}_2(\mathbf{x},t)$ are compared on a 120×120 regular mesh at $t = 2$ and $t = 8.8$. As shown in Fig. 7, every scheme is able to capture the solution at $t = 2$ without any significant difference with the asymptotic solution.

Differences are observed at $t = 8.8$. Upwind Roe schemes (Figs. 7d and f) have damped the high spatial frequencies of the density variation. The global field distribution is predicted coarsely but the lamellar structure of $\mathcal{R}_2$ is lost, the second-order scheme being less accurate than the WENO scheme. This is not the case with the second-order implicit centered scheme (Figs. 7b and 7c) that captures the lamellar structure rather well, especially close to the corners, whereas, as expected with the test mesh, these variations are damped near the middle of the walls. As an intermediate behavior, the filtered fourth-order PADE scheme (Fig. 7e) is able to capture the structure of the $\mathcal{R}_2$ field everywhere except very close to the corners where the oscillations are damped. These comparisons show that the spatial dissipative properties of the scheme plays a significant role in their ability to reproduce the correct behavior for $\mathcal{R}_2$. The two centered schemes (implicit centered scheme and PADE scheme) give the best results since they have the least dissipative error as seen in Section 3.5. More precise results are obtained using the implicit centered scheme, presumably because of the absence of high-order filtering.

It should be noted that the solution plotted here for $M = 0.1$ is identical to the one obtained at $M = 0.01$, up to $t = 8.8$, showing that this solution is not affected significantly by acoustic fluctuations as expected from the asymptotic solution.

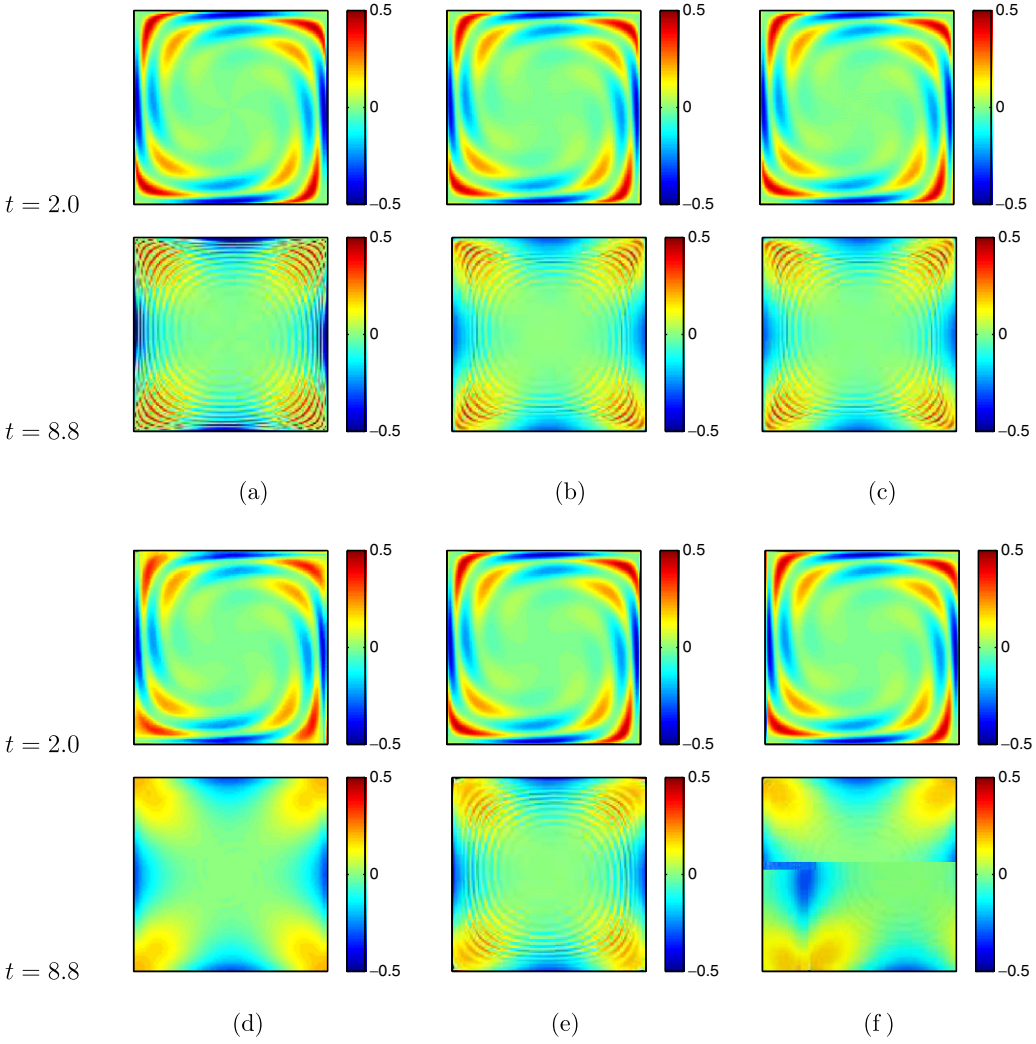

Fig. 7. Slow time part $\mathcal{R}_2$ (Eq. (64)) of density on 120×120 meshes: (a) asymptotic solution (Eq. (65)), (b) implicit centered scheme at CFL = 0.6, (c) implicit centered scheme at CFL = 10.0, (d) Roe–Turkel scheme at CFL = 0.6, (e) filtered fourth-order PADE scheme at CFL = 0.6, (f) fifth-order WENO scheme at CFL = 0.6. Results obtained at $M = 0.1$. Results obtained at $M = 0.01$ are identical.

When CFL = 10.0 is retained with the implicit centered scheme, the same solution is obtained, even though the acoustic contribution has been eliminated from the calculation.

Profiles of $\mathcal{R}_2(\mathbf{x},t)$ along the diagonal of the box are given in Fig. 8 at $t = 8.8$. The particular features noted previously on the 2D plots are also observed on these profiles and the oscillations of $\mathcal{R}_2$ can be compared more accurately. High-order and low-order schemes are able to capture the high frequencies of the density field if their numerical dissipation is small enough. Because of the high-frequency filter applied to the PADE scheme, the oscillations die out near the corners. While being of the second-order, the implicit centered scheme captures the amplitude of the high frequencies oscillations rather well in the entire section. However, a slight phase shift can be observed as compared to the asymptotic solution, a phase that is correctly predicted with the PADE scheme.

Finally, time evolutions of $\mathcal{R}_2(x,y,t)$ are compared in Fig. 9 at $(x = 0.5, y = 0.05)$. The solution given by the second-order implicit centered scheme exhibits the same behavior for CFL = 0.6 and CFL = 10.0 showing that it is not affected by the acoustic fluctuations (Fig. 9a). Results obtained by the other schemes coincide with the asymptotic solution up to $t = 2$, and $\mathcal{R}_2$ values are subjected to a damping effect depending on the dissipative properties of the schemes (Fig. 9b). The second-order Roe–Turkel scheme shows damping of density fluctuations just after $t = 2$ on this mesh, whereas the fifth order WENO scheme allows correct prediction up to $t = 4$. The filtered fourth-order PADE scheme damps the oscillations at $t = 6$, and so does the second-order implicit centered scheme. However, the solution obtained with the implicit centered scheme exhibits a dispersive behavior due to a higher dispersion error and a lower dissipation error at high wavenumber as seen on Section 3.5. It should be mentioned here that the nonlinear Newton solver and the linear solver retained in this study converge enough to have no influence on the spatial solution given by the implicit centered scheme, as shown later in Section 5.4. With the other schemes, the high frequencies of the solution are damped by their spatial dissipative properties, thereby having a stabilizing effect for long time integration. In conclusion, a good spatial distribution of the slow time solution is given by the implicit centered scheme, and high-order schemes (PADE and WENO) show here a more robust time integration behavior.

The influence of the mesh size is illustrated in Fig. 10 where the time evolutions of $\mathcal{R}_2(x,y,t)$ at $(x = 0.5, y = 0.05)$ are given for the different schemes and on the three different meshes 80×80, 160×160 and 320×320. Dissipation errors diminish

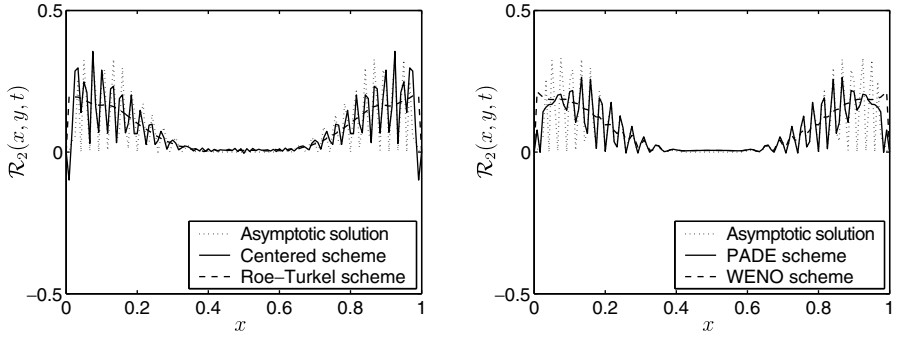

Fig. 8. Profiles of the slow time part $\mathcal{R}_2(x,y,t)$ of density at $t = 8.8$ on the diagonal line $x = 1 - y$. Results obtained at $M = 0.1$. Results obtained at $M = 0.01$ are identical.

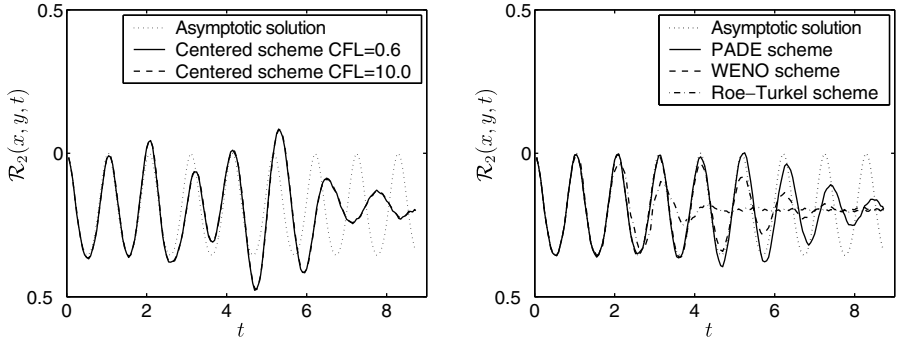

Fig. 9. Time evolution of the slow time part $\mathcal{R}_2$ of density on 120×120 meshes: (a) implicit centered scheme at CFL = 0.6 and at CFL = 10.0 compared to asymptotic solution, (b) fourth-order PADE scheme, fifth-order WENO scheme and Roe–Turkel scheme compared to asymptotic solution at CFL = 0.6. Results obtained at $M = 0.1$. Results obtained at $M = 0.01$ are identical.

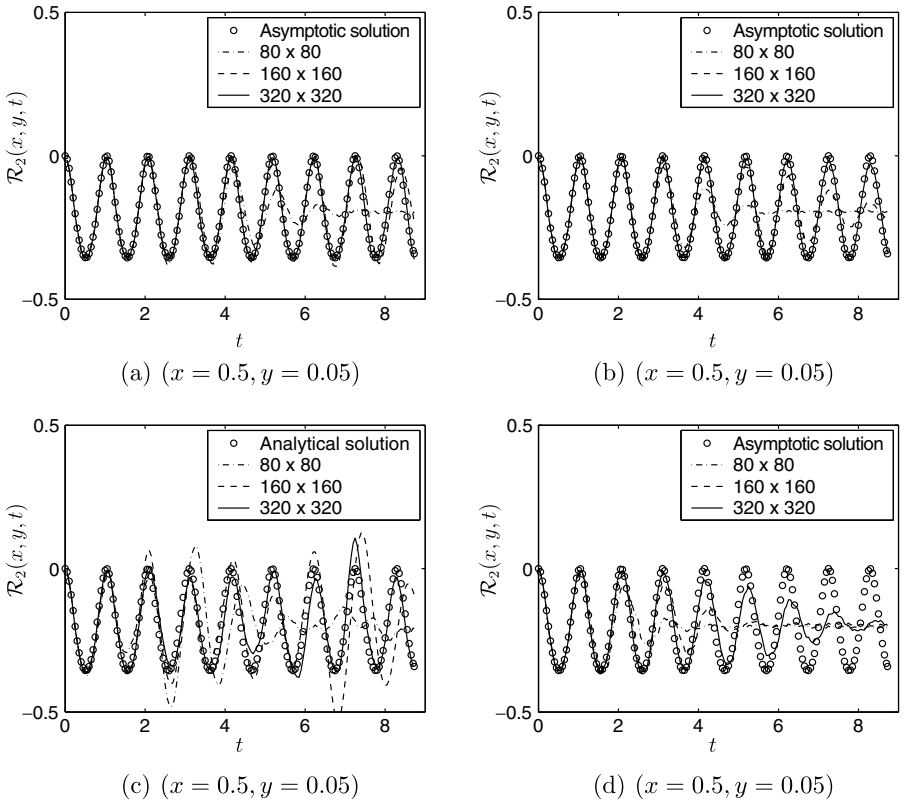

Fig. 10. Influence of mesh resolution on the time evolution of the slow time part $\mathcal{R}_2$ of density: (a) fourth-order PADE scheme, (b) fifth-order WENO scheme, (c) implicit centered scheme, (d) Roe–Turkel scheme. Results obtained at $M = 0.1$. Results obtained at $M = 0.01$ are identical.

with the mesh refinement, allowing the schemes to predict the correct amplitude of the $\mathcal{R}_2(x,y,t)$ oscillations for long time integration. The dispersive nature of the implicit second-order-centered scheme, leading to a phase shift in the oscillations as previously observed, appears later in time with finer meshes, showing a reduction of the numerical error with mesh refinement. The finer mesh of 320×320 nodes however does not allow the implicit scheme (and the Roe–Turkel one) to capture the correct solution up to $t = 8.8$. Numerical error still affects the solution, whereas the 320×320 mesh allows the PADE scheme to match the asymptotic solution at $t = 8.8$ with perfect agreement.

5.3. Numerical prediction of the acoustic part

In order to compare the numerical results at the level of the acoustic fluctuations, the following expression is computed for the two values of M and for the different numerical schemes:

$$\mathcal{P}_3(\mathbf{x},t) \equiv \frac{1}{M^3}\frac{1}{\gamma}[P(\mathbf{x},t) - 1 - M^2\gamma P_2(\mathbf{x})] \tag{66}$$

This expression contains virtually the third and higher order terms of the Mach number expansion. Isovalues of $\mathcal{P}_3$ are compared in Fig. 11 to $\mathcal{P}_3^{as}$ (Eq. (63)) on the 120×120 mesh at $\tau = 5$ for the different schemes.

The high-order schemes give correct results for the $\mathcal{P}_3$ field, with a more accurate prediction of the filtered fourth-order PADE scheme compared to the fifth order WENO scheme. The second-order Roe–Turkel scheme gives the least accurate solution at $M = 0.01$, whereas the implicit scheme captures the acoustic pressure rather well at CFL = 0.6 despite the low order of the scheme. As expected, the acoustic field is not captured at CFL = 10.0 whereas the slow part of the solution at order M^2 appears to be correctly described as shown in the previous section.

The time evolutions of $\mathcal{P}_3$, given in Fig. 12, show that all schemes work correctly on the 120×120 mesh, except the Roe–Turkel scheme (Fig. 12a) at $M = 0.01$. For this scheme, a 320×320 mesh size is required to get an acceptable solution, as illustrated later in Section 5.4. At $M = 0.1$, the behaviors of the schemes are very similar (Fig. 12b). As discussed in Section 4, the influence of the fourth-order terms of the Mach expansion of the pressure is negligible at $M = 0.01$, whereas it is clearly not at $M = 0.1$. It has been checked that the values of the frequencies of the fourth-order term are correctly captured by the different schemes.

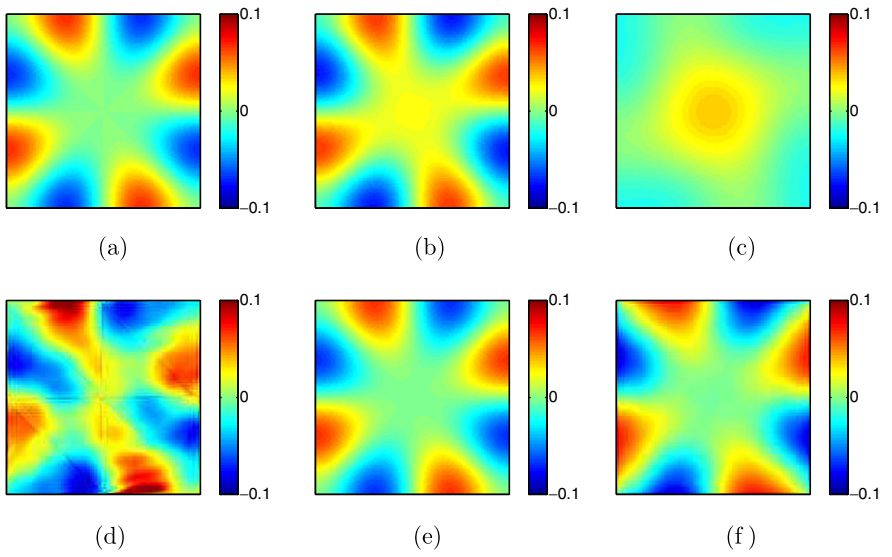

Fig. 11. Acou ssure $\mathcal{P}_3$ (Eq. (66)) on 120 × 120 meshes at $\tau = 5$ for $M = 0.01$: (a) asymptotic solution (Eq. (63)), (b) implicit centered scheme at CFL = 0.6, (c) i centered scheme at CFL = 10.0, (d) Roe–Turkel scheme at CFL = 0.6, (e) fourth-order PADE scheme at CFL = 0.6, (f) fifth-order WENO scheme at CF

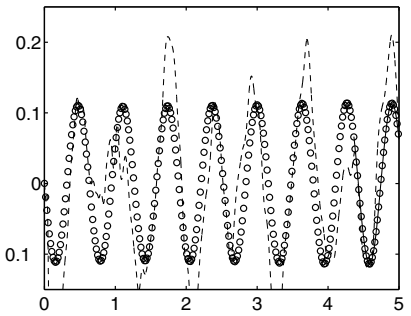

As previously said, the major acoustic contribution is the one associated to the frequency $f_{13} = f_{31}$ of the third-order asymptotic expansion term. The amplitude of this term is extracted from the time evolution of $\mathcal{P}_3(\mathbf{x}, t)$ at ($x = 0.66$, $y = 0.05$) by Hilbert transform and band-pass filtering, as described in Section 4, and compared to the amplitude of $\delta P_3(\mathbf{x}, \tau, 0)$ (Fig. 13). The asymptotic development predicts a constant evolution that is rather well captured by the filtered fourth-order PADE scheme at both Mach numbers. The prediction of the acoustic amplitude however degenerates for the fifth order WENO scheme at $M = 0.01$ compared to $M = 0.1$. second-order upwind schemes are well known to be not accurate enough for low Mach number acoustic predictions, and this result is verified in the evolution of the acoustic amplitude given by the Roe–Turkel scheme at $M = 0.01$. Convergence of the acoustic part worsens as the Mach number decreases, the solution here not being grid independent. The implicit scheme exhibits a surprisingly good ability to capture the acoustic part, even if a reduction of the acoustic intensity occurs in time that is more pronounced at small Mach numbers. As already noticed in Section 4, wiggles do appear in Fig. 13, that are due to the coarse filtering of the additional frequencies. Moreover, a slight windowing effect is visible close to $t = 0$ and $t = 8.8$, but this has no effect on the global analysis of the acoustic amplitude evolution.

5.4. Influence of the low Mach number treatment

The influence of preconditioning on the second-order Roe scheme is illustrated by the time evolution of $\mathcal{R}_2$ in Fig. 14. The unpreconditioned scheme exhibits more numerical dissipation that damps out the variations of the density a little sooner for both Mach number cases. Larger differences occur in the time evolution of the acoustic pressure $\mathcal{P}_3$ as shown in Fig. 15.

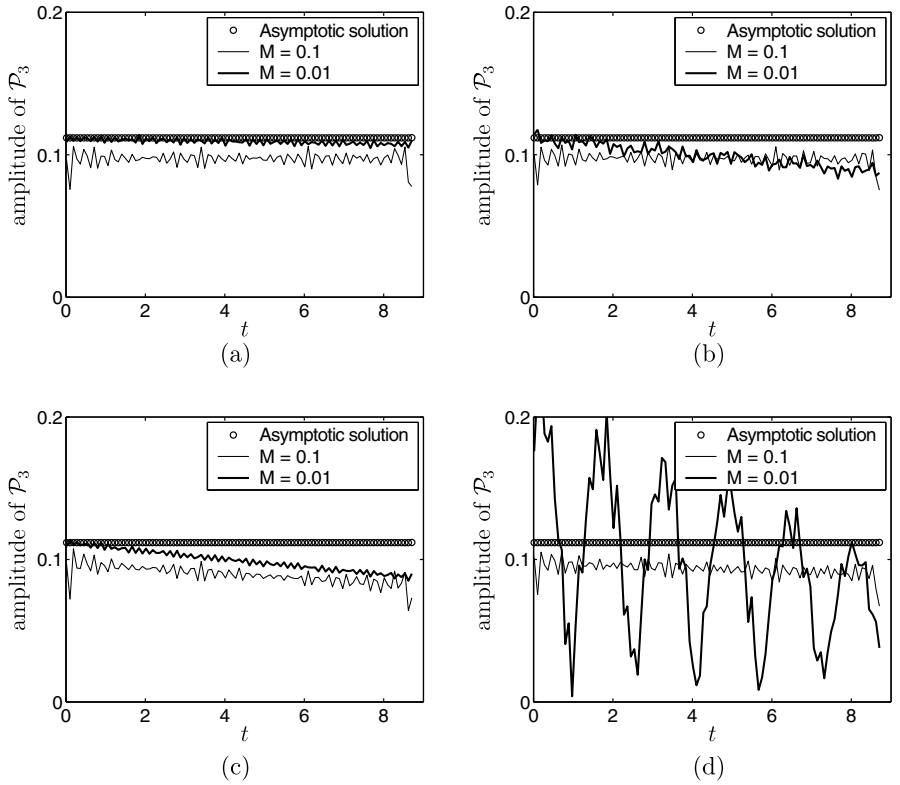

Fig. 13. Time evolution of the acoustic signal amplitude at ($x = 0.66$,$y = 0.05$) up to $t = 8.8$: (a) filtered fourth-order PADE scheme, (b) fifth-order WENO scheme, (c) implicit second-order-centered scheme, (d) second-order Roe–Turkel scheme.

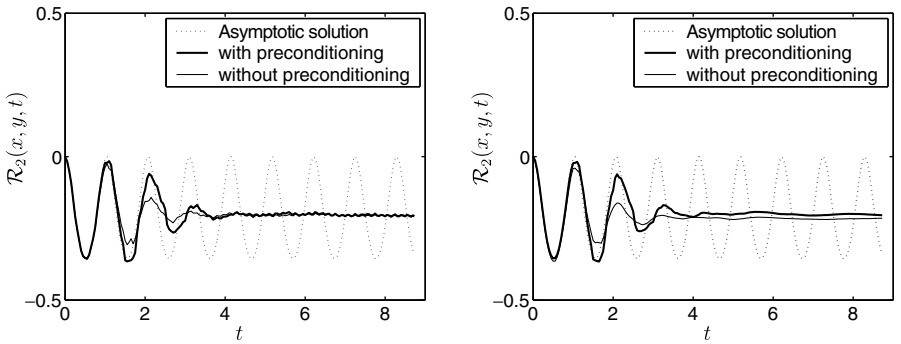

Fig. 14. Influence of preconditioning on the time evolution of $\mathcal{R}_2(x, y, t)$ at ($x = 0.5$, $y = 0.05$) for the second-order Roe–Turkel scheme.

While at $M = 0.1$, the evolution is well captured, at $M = 0.01$ on a 320×320 mesh where the solution is mesh-independent, the small perturbations seen with the preconditioned scheme are dramatically amplified without preconditioning.

For the implicit centered scheme, the low Mach number treatment has a great influence on the solution of the nonlinear steps. When the low Mach number pressure decomposition (see Section 3.4) is used, the residual of the energy equation at the beginning of each nonlinear iteration is independent of the Mach number, and is of the same order of magnitude as those of the other equations. On the contrary, when this pressure decomposition is not used, the initial residual of the energy equation is much larger ($\sim 10^2$ at $M = 0.1$ and $\sim 10^4$ at $M = 0.01$) and varies as M^{-2}. When using convergence criteria independent of the Mach number, as specified in the introduction to Section 5, the coupled implicit system is solved with sufficient accuracy for all the variables to converge towards the solution when the pressure decomposition is applied. Conversely, without this decomposition, the total energy is not calculated accurately. At $M = 0.1$, small wiggles can be observed for long time integration and, at $M = 0.01$, these spurious oscillations become more severe and finally lead the simulation to diverge with time.

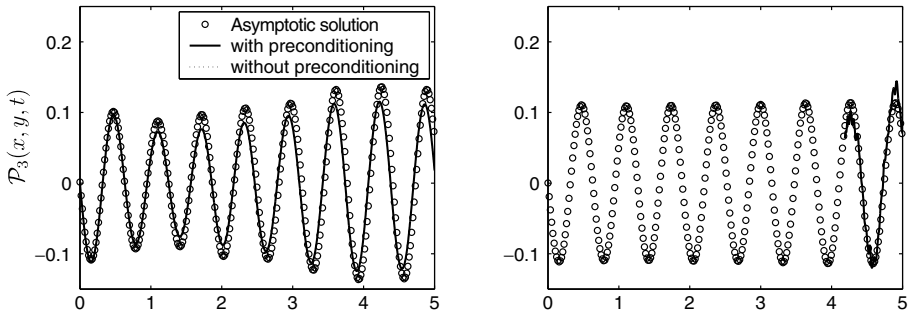

(a) $M = 0.1$ at $CFL = 0.6$

This problem can be partially overcome by increasing the CFL number, because then, the implicit solver damps out the highest frequencies and captures the low ones more efficiently.

Identical solutions can be predicted with and without pressure decomposition when appropriate convergence criteria are applied. With pressure decomposition, a same reduction of the nonlinear (resp. linear) residuals by 6 (resp. 9) orders has been shown to be suitable, for $M = 0.1$ and $M = 0.01$. Without pressure decomposition, the equivalent criteria would be to reduce by 8 (resp. 11) orders the residuals at $M = 0.1$ and by 10 (resp. 13) orders the ones at the $M = 0.01$. In that case the number of nonlinear (and linear) iterations increases considerably and the CPU time is twice larger than in the case when the decomposition is used.

This shows that the low Mach number treatment is crucial in the ability of the second-order schemes to predict efficiently the slow time variation of the solution at low Mach number.

5.5. Computational cost

Table 2 gives the CPU time needed for the studied schemes. When comparing the computational costs, it should be taken into account that the corresponding schemes are not implemented in a single code, and that the characteristics of the codes in terms of architecture and optimization are very different. The major difference lies in the unstructured versus structured approaches, the first one being dedicated to intensive parallel computing, whereas the latter is extensively vectorized. The most efficient code is the structured explicit PADE scheme, which also gives the most accurate solutions. Comparing the two Roe schemes gives an indication about the additional cost of the unstructured approach, which is about seven times more expensive than the structured one. Using the implicit time integration costs about twice the time of the explicit solver at high Mach numbers. However, for lower values of the Mach number the efficiency of the implicit method increases. The weaker coupling of the total energy with the other conservative variables at small Mach numbers makes the nonlinear iterations converge more rapidly at $M = 0.01$ than at $M = 0.1$. Faster solutions are obtained by increasing the CFL number, even if in that case, the convergence rate of the linear systems decreases. The condition number of the matrices has been estimated numerically and has been found to increase with the CFL number and to vary as $O(M^{-2})$ at CFL = 0.6 and CFL = 10. However, the Mach number does not influence the number of iterations required by the linear solver GMRES, despite the fact that the condition number of the matrix evolves as $O(M^{-2})$.

6. Conclusion

The inviscid low Mach number compressible flow which develops from the plane Taylor incompressible vortex with constant density has been studied. A reference solution for this model flow has been obtained by a two-time scale asymptotic expansion in the zero Mach number limit and has been analyzed for two Mach number values, $M = 0.1$ and $M = 0.01$. The initial flow is a steady solution for the incompressible Euler equations but not for the compressible ones, accordingly, all variables appear to vary in space and time, because of the conservation of entropy in the compressible flow. Time evolution and Mach number dependency of the density and pressure fields have been analyzed with the help of the asymptotic expansion. The asymptotic expansion shows that the flow varies on two separate time scales, one is the slow convective and the other is the fast acoustic time scale. Because of the initial conditions retained in our model flow, the Mach number dependence appears only from $O(M^2)$ terms. At this order, the variations of density that are generated in the flow do not depend on the fast time scale. Acoustic fluctuations appear only from the third-order term. At this order, pressure fluctuations do not depend on the slow time.

A selection of numerical schemes, based on separate time and space integration has been implemented to simulate this flow. The ability of the schemes to predict the low Mach number flow developing from the plane Taylor incompressible vortex has been analyzed.

The first scheme belongs to the class of explicit second-order Roe schemes, with a Turkel preconditioning of the Jacobian Euler flux matrix. It is the most dissipative scheme of the selection and consequently the least accurate and also the more robust one for the simulations at low Mach numbers. Very fine meshes are required to obtain reasonable predictions of the slow time density variations that otherwise would be rapidly damped in space. Acoustic pressure suffers from a lack of accuracy at low Mach numbers.

Two explicit high-order compressible schemes have been compared, a fifth order WENO-Roe one and a fourth-order filtered compact PADE one. Both schemes are analyzed without any specific treatment of the low Mach number limit. They have shown their ability to correctly predict the slow time density variations with reasonable damping of the high spatial frequencies on a rather coarse mesh size. The filtered PADE scheme being less dissipative than the WENO-Roe upwind scheme, it gives better results. Both schemes are robust even if the application of a spatial filter to the centered compact PADE scheme is necessary to deal with the high spatial frequencies of the density field variations. The PADE scheme is shown to be the best scheme to capture the main variations of the acoustic pressure on long time integration at the smaller Mach number.

Despite its low order of discretization, the implicit centered implicit scheme has proved to be able to capture the low Mach density variations without dissipation but with a small dispersion error. When used with a CFL number larger than one, acoustic fluctuations are eliminated from the solution whereas, for CFL < 1, reasonable acoustic pressure levels are obtained. This second-order-centered implicit scheme needs a pressure decomposition to overcome the cancellation errors when solving the linear and nonlinear systems in order to simulate such low Mach number flows efficiently. It is interesting to obtain rather precise results with second-order schemes in view of applications to complex flow configurations.

To summarize, compact schemes like the PADE scheme are the most accurate ones, especially in the prediction of the acoustic flow field. Finite volume implicit centered schemes allow larger time steps while preserving the global accuracy of the flow variables if knowledge of the acoustic field is not required. A promising prospect would therefore be to develop implicit high-order finite volume centered schemes to combine the advantage of both approaches, e.g. in the spirit of the work of Visbal and Gaitonde [58] for the finite difference schemes.

Acknowledgment

Simulations were been performed on the computers of the Fédération Lyonnaise de Calcul Haute Performance and on the machines of the CINES (Centre Informatique National de l'Enseignement Supérieur).

References

[1] I.A. Abramowitz, M. Stegun, Handbook of Mathematical Functions with Formulas, Graphs, and Mathematical Tables, ninth Dover printing, tenth GPO printing ed., Dover, New York, 1964.
[2] T. Alazard, Incompressible limit of the nonisentropic Euler equations with the solid wall boundary conditions, Adv. Differential Equations 1 (2005) 19–44.
[3] G. Ali, Low Mach number flows in time-dependent domain, SIAM J. Appl. Math. 63 (2003) 2020–2041.
[4] K. Asano, On the incompressible limit of the compressible Euler equation, Jpn. J. Appl. Math. 4 (1987) 455–488.
[5] S. Balay, K. Buschelman, W. Gropp, D. Kaushik, M. Knepley, L.C. McInnes, B. Smith, H. Zhang, Portable, extensible toolkit for scientific computation web page, 2001. <http://www.mcs.anl.gov/petsc>.
[6] F. Bartlmä, The transition from slow burning to detonation, Acta Astronaut. 6 (1979) 435–447.
[7] F. Beux, M.-V. Salvetti, A. Ignatyev, D. Li, C. Merkle, E. Sinibaldi, A numerical study of non-cavitating and cavitating liquid flow around a hydrofoil, M2AN 39 (2005) 577–590.
[8] H. Bijl, P. Wesseling, A unified method for computing incompressible and compressible flows in boundary-fitted coordinates, J. Comput. Phys. 141 (1998) 153–173.
[9] P. Birken, A. Meister, Stability of preconditioned finite volume schemes at low mach numbers, Math. Statist. 45 (2005) 463–480.
[10] D. Bresch, M. Gisclon, C.-K. Lin, An example of low Mach number effects for compressible flows with nonconstant density limit, M2AN 39 (2005) 477–487.

[11] W. Briley, H. McDonald, S. Shamroth, A low Mach number Euler formulation and application to time-iterative LBI schemes, AIAA J. 21 (10) (1983) 1467–1469.
[12] W. Briley, L. Taylor, D. Whitfield, High-resolution viscous flow simulations at arbitrary Mach number, J. Comput. Phys. 184 (2003) 79–105.
[13] A. Cadiou, NadiaLES: manuel théorique, Tech. Rep., Note technique CODICIEL LMFA 2003-01, 2003.
[14] A. Cadiou, C. Tenaud, Implicit WENO shock capturing scheme for unsteady flows. application to one-dimensional euler equations, Int. J. Numer. Methods Fluids 45 (2004) 197–229.
[15] R. Carpentier, Approx. et analyse numérique d'ecoulements instationnaires, Ph.D. thesis, Université de Nice Sofia-Antipolis, 1995.
[16] Y.-H. Choi, C. Merkle, The application of preconditioning in viscous flows, J. Comput. Phys. 105 (1993) 207–223.
[17] L. Dailey, R. Pletcher, Evaluation of multigrid acceleration for preconditioned time-accurate Navier–Stokes algorithms, Comput. Fluids 25 (1996) 791–811.
[18] V. Daru, C. Tenaud, High order one-step monotonicity-preserving schemes for unsteady compressible flow calculations, J. Comput. Phys. 193 (2004) 563–594.
[19] A. Dervieux, J. Désidéri, Compressible flow solvers using unstructured grids., Tech. Rep., Technical Report RR 1732, 1992.
[20] B. Desjardins, E. Grenier, Low Mach number limit of viscous compressible flows in the whole space, Proc. R. Soc. Lond. 455 (1999) 2271–2279.
[21] L. Duchamp de Lageneste, Simulation des grandes echelles d'ecoulements compressibles et réactifs sur maillages non-structurés, Ph.D. thesis, École Centrale de Lyon, 1999.
[22] K. Feldman, Review of the literature on Rijke thermoacoustic phenomena, J. Sound Vib. 7 (1968) 83–89.
[23] H. Guillard, C. Viozat, On the behaviour of upwind schemes in the low Mach number limit, Comput. Fluids 28 (1999) 63–86.
[24] M. Hubbard, P. Roe, Compact high-resolution algorithms for time-dependent advection on unstructured grids, Int. J. Numer. Methods Fluids 33 (2000) 711–736.
[25] H. Isozaki, Wave operators and the incompressible limit of the compressible Euler equation, Commun. Math. Phys. 110 (1987) 519–524.
[26] P. Jenny, B. Müller, Convergence acceleration for computing steady-state compressible flow at low Mach numbers, Comput. Fluids 28 (1999) 951–972.
[27] G. Jiang, C. Shu, Efficient implementation of weighted ENO schemes, J. Comput. Phys. 126 (1996) 202–228.
[28] I. Keshtiban, F. Belblidia, M. Webster, Compressible flow solvers for low Mach number flows – a review, Csr 2, Institute of non-Newtonian fluid mechanics, Department of Computer Science, University of Wales, Swansea, 2004.
[29] S. Klainerman, A. Majda, Singular limits of quasilinear hyperbolic systems with large parameters and the incompressible limit of compressible fluids, Commun. Pure Appl. Math. 34 (1981) 481–524.
[30] S. Klainerman, A. Majda, Compressible and incompressible fluids, Commun. Pure Appl. Math. 35 (1982) 629–653.
[31] R. Klein, Semi-implicit extension of a Godunov-type scheme based on low Mach number asymptotics I: One-dimensional flow, J. Comput. Phys. 121 (1995) 213–237.
[32] H.-O. Kreiss, J. Lorentz, M. Naughton, Convergence of the solutions of the compressible to the solution of the incompressible Navier–Stokes equations, Adv. Appl. Math. 12 (1991) 187–214.
[33] B.V. Leer, Towards the ultimate conservative difference scheme III. Upstream centered finite difference schemes for ideal compressible flow, J. Comput. Phys. 23 (1977) 263–275.
[34] P.-L. Lions, N. Masmoudi, Incompressible limit for a viscous compressible fluid, J. Math. Pure Appl. 77 (1998) 585–627.
[35] A. Majda, J. Sethian, The derivation and numerical solution of the equations for zero Mach number combustion, Combust. Sci. Technol. 42 (1985) 185–205.
[36] A. Meister, Asymptotic single and multiple scale expansions in the low Mach number limit, SIAM J. Appl. Math. 60 (1999) 256–271.
[37] C. Merkle, Y.-H. Choi, Computation of low-speed compressible flows with heat addition, AIAA J. 25 (6) (1987) 831–838.
[38] C. Merkle, Y.-H. Choi, Computation of low-speed compressible flows with time-marching procedure, Int. J. Numer. Methods Eng. 25 (1988) 293–311.
[39] G. Métivier, S. Schochet, The incompressible limit of the non-isentropique Euler equations, Arch. Ration. Mech. Anal. 158 (2001) 61–90.
[40] B. Müller, Low Mach number asymptotics of the Navier–Stokes equations and numerical implications, in: VKI Lecture Series 1999–03, 1999.
[41] C.-D. Munz, M. Dumbser, S. Roller, Linearized acoustic perturbation equations for low Mach number flow with variable density and temperature, J. Comput. Phys. 224 (2007) 352–364.
[42] K. Paillère, C. Viozat, A. Kumbaro, I. Toumi, Comparison of low Mach number models for natural convection problems, Heat Mass Transfer 36 (2000) 567–573.
[43] J.M.C. Pereira, J.C.F. Pereira, Fourier analysis of several finite difference schemes for the one-dimensional unsteady convection-diffusion equation, Int. J. Numer. Methods Fluids 36 (2001) 417–439.
[44] C.L. Ribault, L.L. Penven, M. Buffat, LES of the compressed Taylor vortex flow using a finite volume/finite element method on unstructured grids, Int. J. Numer. Methods Fluids 52 (4) (2006) 355–379.
[45] P. Roe, Approximate Riemann solvers, parameters, vectors and difference schemes, J. Comput. Phys. 43 (1981) 357–372.
[46] S. Roller, C. Munz, A low Mach number scheme based on multi-scale asymptotics, Comput. Visualiz. Sci. 3 (2000) 85–91.
[47] S. Schochet, Asymtotics for symmetric hyperbolic systems with a large parameter, J. Differential Equations 75 (1988) 1–27.
[48] S. Schochet, The mathematical theory of low Mach number flow, M2AN 39 (2005) 441–458.
[49] J. Sesterhenn, B. Müller, H. Thomann, On the cancellation problem in calculating compressible low Mach number flows, J. Comput. Phys. 151 (1999) 597–615.
[50] C. Shu, Essentially non-oscillatory and weighted essentially non-oscillatory schemes for hyperbolic conservation laws, Tech. Rep. 65, ICASE 97-65, 1997.
[51] W. Shu, S. Osher, Efficient implementation of essentially non-oscillatory shock capturing schemes, J. Comput. Phys. 77 (1988) 439–471.
[52] J.-S. Shuen, K.-H. Chen, Y. Choi, A coupled implicit method for chemical non-equilibrium flows at all speeds, J. Comput. Phys. 106 (1993) 306–318.
[53] M. Toledo, L.L. Penven, M. Buffat, A. Cadiou, J. Padilla, Large eddy simulation of the generation and breakdown of a tumbling flow, Int. J. Heat Fluid Flow 28 (2007) 113–126.
[54] E. Turkel, Preconditioned methods for solving the incompressible and low speed compressible equations, J. Comput. Phys. 72 (1987) 277–298.
[55] E. Turkel, Preconditioning techniques in computational fluid dynamics, Annu. Rev. Fluid Mech. 31 (1999) 385–416.
[56] D. van der Heul, C. Vuik, P. Wesseling, A conservative pressure-correction method for flow at all speeds, Comput. Fluids 32 (2003) 1113–1132.
[57] M. Visbal, D. Gaitonde, High-order accurate methods for complex unsteady subsonic flows, AIAA J. 37 (10) (1999) 1231.
[58] M. Visbal, D. Gaitonde, On the use of higher-order finite difference schemes on curvilinear and deforming meshes, J. Comput. Phys. 181 (2002) 155–185.
[59] J. Wong, D. Darmofal, J. Peraire, The solution of the compressible Euler equations at low Mach numbers using a stabilized finite element algorithm, Comput. Methods Appl. Eng. 190 (2001) 5719–5737.
[60] G. Zank, W. Matthaeus, The equations of nearly incompressible fluids I. Hydrodynamics, turbulence, and waves, Phys. Fluids 1 (1991) 69–82.
[61] R. Zeytounian, Theory and Applications of Nonviscous Fluid Flows, Springer-Verlag, 2002.
[62] R. Zeytounian, Theory and Applications of Viscous Fluid Flows, Springer-Verlag, 2004.